



The Genesis of the Askartor Be-Mo Deposit in the North Xinjiang, Northwest China: Evidence From Geology, Geochemistry, U-Pb, and Re-Os Geochronology

Tang Yong ^{*}, Zhang Hui ^{*} and Lv Zheng-Hang

Key Laboratory for High Temperature and High-Pressure Study of the Earth's Interior, Institute of Geochemistry, Chinese Academy of Sciences, Guiyang, China

OPEN ACCESS

Edited by:

Chang-Zhi Wu,
Chang'an University, China

Reviewed by:

Fuquan Yang,
Chinese Academy of Geological Sciences (CAGS), China

Rui Wang,
China University of Geosciences,
China

*Correspondence:

Tang Yong
tangyong@vip.gyig.ac.cn
Zhang Hui
zhanghui@vip.gyig.ac.cn

Specialty section:

This article was submitted to
Economic Geology,
a section of the journal
Frontiers in Earth Science

Received: 28 December 2020

Accepted: 03 February 2021

Published: 16 March 2021

Citation:

Yong T, Hui Z and Zheng-Hang L (2021) The Genesis of the Askartor Be-Mo Deposit in the North Xinjiang, Northwest China: Evidence From Geology, Geochemistry, U-Pb, and Re-Os Geochronology. *Front. Earth Sci.* 9:646772.
doi: 10.3389/feart.2021.646772

The Askartor Be-Mo deposit is located in the southeastern area of the Chinese Altay orogenic belt in Xinjiang, NW China. Zircon U-Pb data show that there are two periods of magmatic activities in the Askartor Be-Mo ore district, namely, the Devonian granodiorite (386.8 ± 2.6 Ma) and biotite granite (385.4 ± 4.4 Ma), and the Triassic two-mica granite (247.5 ± 2.2 Ma) and muscovite granite (231.4 ± 2.0 Ma). The zircon U-Pb age of pegmatoid orebody is 220.6 ± 1.6 Ma which coincides with the molybdenite Re-Os isochron age of 228.7 ± 7.1 Ma. The two-mica and muscovite granites belong to the high-K Calc-alkaline series with peraluminous features, and are characterized by high SiO_2 (71.92–75.41 wt%), and Al_2O_3 (13.43–15.98 wt%), and low TiO_2 (0.01–0.25 wt%), Fe_2O_3 (0.11–1.14 wt%) and CaO (0.07–0.76 wt%). The highly fractionated element ratios of Y/Ho , Zr/Hf and Nb/Ta , and the rare earth element tetrad effect occur in the muscovite granite, indicating the fluid exsolution occurs at the late stage of magma evolution, and the muscovite granite experienced the strong self-metasomatism. Rayleigh fractional calculations show that the Askartor Be-Mo deposit is the product of multistage fractional crystallization of initial Be-enriched magma.

Keywords: Askartor Be deposit, U-Pb age, tetrad effect, melt-fluid interaction, NW China

INTRODUCTION

Because of its unique physical and chemical properties, beryllium (Be) is widely used in many important industrial products used in the aerospace, computer, defense, medical, nuclear, and telecommunications industries. The two most important Be ores are bertrandite [$\text{Be}_2\text{Si}_2\text{O}_7(\text{OH})_2$] and beryl [$\text{Be}_3\text{Al}_2\text{Si}_6\text{O}_{18}$]. At present, 90% of the source mineral of the world's beryllium produce comes from bertrandite, but industrial beryl is critical for the production of the very high purity beryllium metal needed for some strategic applications (Foley et al., 2017). At present, two distinct classes of deposits currently account for most beryllium ores (Barton and Young, 2002; London and Evensen, 2002): they are 1) volcanic and carbonated-hosted deposits that contain the mineral bertrandite, and 2) pegmatite-type deposits that have an abundance of the mineral beryl.

The Chinese Altay orogen, located in Northwest China, is the most important beryllium ore belt in China. Its deposit is mainly pegmatite type. The geological characteristics (Zou and Li, 2006; Qin et al., 2013; Yang et al., 2018; Zhang et al., 2019), geochronology (Wang et al., 2007; Chen, 2011; Ren

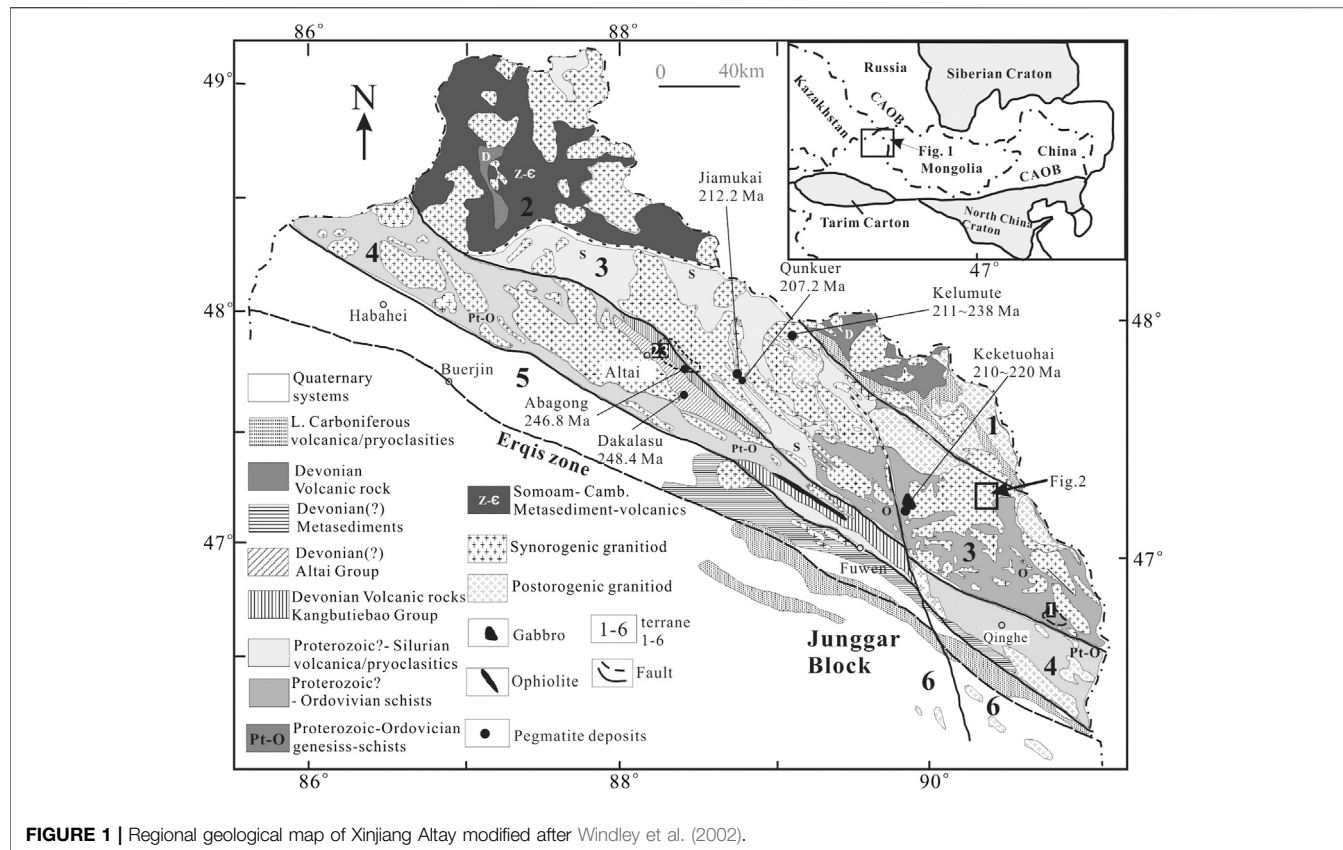


FIGURE 1 | Regional geological map of Xinjiang Altay modified after Windley et al. (2002).

et al., 2011; Lv et al., 2012) and internal evolution (Zhang et al., 2008; Lv et al., 2012; Stepanov and Hermann, 2013; Yin et al., 2013) of pegmatites in this area have been studied systematically. However, the mechanism of extraordinary enrichment of beryllium in pegmatites is not clear. Based on the solubility of beryl and the partition coefficient of Be, Evensen and London (2002) considered that extended fractionation beyond 90% total solidification by at least a three-step process is required to achieve beryl saturation in granitic magma systems, but there is a lack of factual evidence.

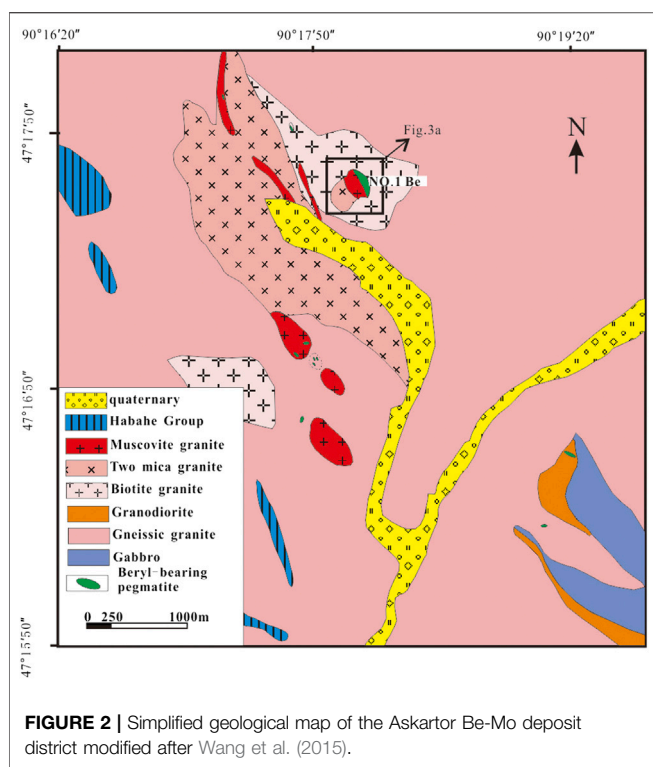
The Askartor deposit is the only granite-related Be-Mo deposit in the Chinese Altay orogen. The Askartor granite pluton is a composite rock body with obvious vertical zoning, from bottom to top, the rock types change from two-mica granite, through muscovite granite, to pegmatite. In addition, there are granodiorite and biotite granite in the ore district. Zou and Li (2006) presented the geological features, and ore body morphology. The ages of different rock types have been presented by Wang et al. (2015), Ding et al. (2016), Zhang et al. (2017). However, the processes that might have contributed to the genesis of this deposit have not been noticed. Therefore, in this study, we have carried out a systemic study of the geology, geochronology, and geochemistry, in order to establish the mineralization model of the Askartor Be-Mo deposit, and identify the key factors restricting the enrichment of Be.

GEOLOGICAL BACKGROUND

Regional Geology

The Altay orogen, which is the southernmost part of the Central Asian Orogenic Belt (CAOB), is situated between the south Siberian Craton to the north and the Junggar Block to the south. According to Windley et al. (2002), the Altay orogen in China is composed of the following six terranes, and details of the terranes can be found in Windley et al. (2002). The rare metal deposits are mainly distributed in Terrane 3 and Terrane 4 (Figure 1).

Recent studies have showed that the Chinese Altay orogen blet is a subduction-related accretionary orogen blet. The tectonic setting of the Chinese Altay varied from a passive continental margin to active continental margin during the Middle Cambrian, and then, it underwent a prolonged subduction process from Ordovician to Carboniferous, characterized by massive magma activities, and high-temperature metamorphism (e.g., Sun et al., 2008; Jiang et al., 2010; Cai et al., 2010; Cai et al., 2011a; Cai et al., 2012a; Cai et al., 2011b). During the Permian period, the Chinese Altai converged consecutively with the East and West Junggar arcs because of the closure of the Paleo-Asian Ocean (e.g., Cai et al., 2012b; Li et al., 2015; Cai et al., 2016; Broussolle et al., 2018). Since the Triassic period, the Chinese Altai has entered into a post-orogenic stage After the amalgamation of the Siberia and Tarim



cratons (e.g., Xiao et al., 2008; Xiao et al., 2009; Xiao et al., 2015; Cai et al., 2016; Xiao et al., 2018).

The granitoids occupy over ~40% of the Chinese Altay orogen (Zou et al., 1988). High precision U-Pb dating results of LA-ICPMS, SHRIMP, and SIMS shows that most of the granitoids were emplaced during the Early to Middle Paleozoic time, with minor ones in the Permian period (Zou et al., 1988; Chen and Jahn, 2002; Wang et al., 2006; Yuan et al., 2007; Sun et al., 2008). The Early Middle Paleozoic I and S-type granitoid, which is emplaced from 507 to 360 Ma, display arc-related geochemical characters (Yuan et al., 2007; Wang et al., 2009; Cai et al., 2011a, Cai et al., 2011b). They are usually deformed and partly metamorphosed to become foliated (Wang et al., 2009). In contrast, the A or I-type granitoids emplaced at ca. 290–250 Ma are mostly undeformed and possess within-plate geochemical characteristics (Tong et al., 2014).

The Chinese Altay orogen is an important rare metal metallogenic belt in China, and its deposit is mainly pegmatite. Approximately 100,000 pegmatite dykes exposed in the Chinese Altay (Zou and Li, 2006). These pegmatite dykes formed during the Devonian synorogenic to Jurassic post-orogenic to anorogenic stage, and mostly concentrated in Triassic (e.g., Ren et al., 2011; Lv et al., 2021 and references therein). The Askartor Be-Mo deposit is the only rare metal deposit related to granite.

Geology of the ore District

The Arskartor Be deposit is located in the southeastern of the Central Altay, and about 80 km north of the Qinghe County (**Figure 1**). This deposit has mined since 1954, and a total of

11,200 tons of ore, which occupy only 2% of the total reserves, have been produced until 1996.

The Upper Ordovician Habahe subgroup sporadically crops out in the mining area, and is composed of biotite-quartz schist and biotite gneiss. Magmatic rocks develop well and make up 95% of the whole mining area, including granodiorites, biotite granites, two mica granites, and medium-fine grain muscovite granites (**Figure 2**). Granodiorites are the most voluminous of these intrusive rocks. These rocks are grey-black, fine to medium-grained, with a massive texture. They are composed of quartz (20–25 vol%), plagioclase (50 vol%), K-feldspar (\pm 10 vol%), and biotite (10–15 vol%). Accessory minerals include zircon, apatite, titanite, and magnetite. Biotite granites are the ore-hosting rock, with an outcrop area of about 0.9 km². These biotite granites are grey-white, and have an unequal-particle hypidiomorphic structure with a massive texture. Petrographic observation shows that the mineral compositions mainly involve quartz (30–35 vol%), plagioclase (\pm 40 vol%), K-feldspar (\pm 15 vol%), biotite (5–10 vol%), and muscovite (\pm 2 vol%). Biotite granites are intruded by two mica granites, and the boundary between those two intrusions is sharp and clear. The surface outcrop of the two mica granites is up to 5 km². They are grey-white, and have a medium-to coarse grain granitic structure with a massive texture. The two mica granites are mainly composed of quartz (35 vol%), plagioclase (~35 vol%), K-feldspar (20 vol%), biotite (\pm 5 vol%), and muscovite (\pm 5 vol%). Muscovite granites occur in the upper portion of the two mica granites, and the transition between both granite types is gradational. The Muscovite granites have a fine-to medium-grain granitic structure. These rocks are mainly composed of quartz (30–35 vol%), plagioclase (35 vol%), K-feldspar (\pm 20 vol%), and muscovite (5–10 vol%).

The Askartor Be-Mo deposit is composed of primary ore and placer. The primary ore consists of pegmatoid-type beryllium ore body in the upper part and granitite-type beryllium ore body in the lower part, and the two parts show a gradual transitional relationship. Detailed surface geological mapping, underground mining workings and drill holes demonstrate that the following six zones are successively encountered from bottom to top (**Figure 3**):

- (1) medium-to fine-grain muscovite granite. These rocks are mainly composed of quartz (30–35 vol%), plagioclase (35 vol%), K-feldspar (\pm 20 vol%), and muscovite (5–10 vol%).
- (2) beryl-bearing fine-grain albited muscovite granite. They are grey-white, and have a fine-grain granitic structure with a massive texture. These rocks are mainly composed of quartz (30–35 vol%), albite (\pm 40 vol%), K-feldspar (\pm 20 vol%), and muscovite (\pm 10 vol%). Beryl sporadically occurs in these rocks.
- (3) banded muscovite-quartz-albite zone (**Figures 4A,B**). This zone is usually 4~5 m wide, 0.1~2 m long and spans 10 m at its widest place. Meanwhile, it has a strong Be-mineralization and a gradual transition relationship with fine-grained albited muscovite granitite zone. Albite, microcline, quartz, muscovite, and beryl formed the zone's clear banded structure.

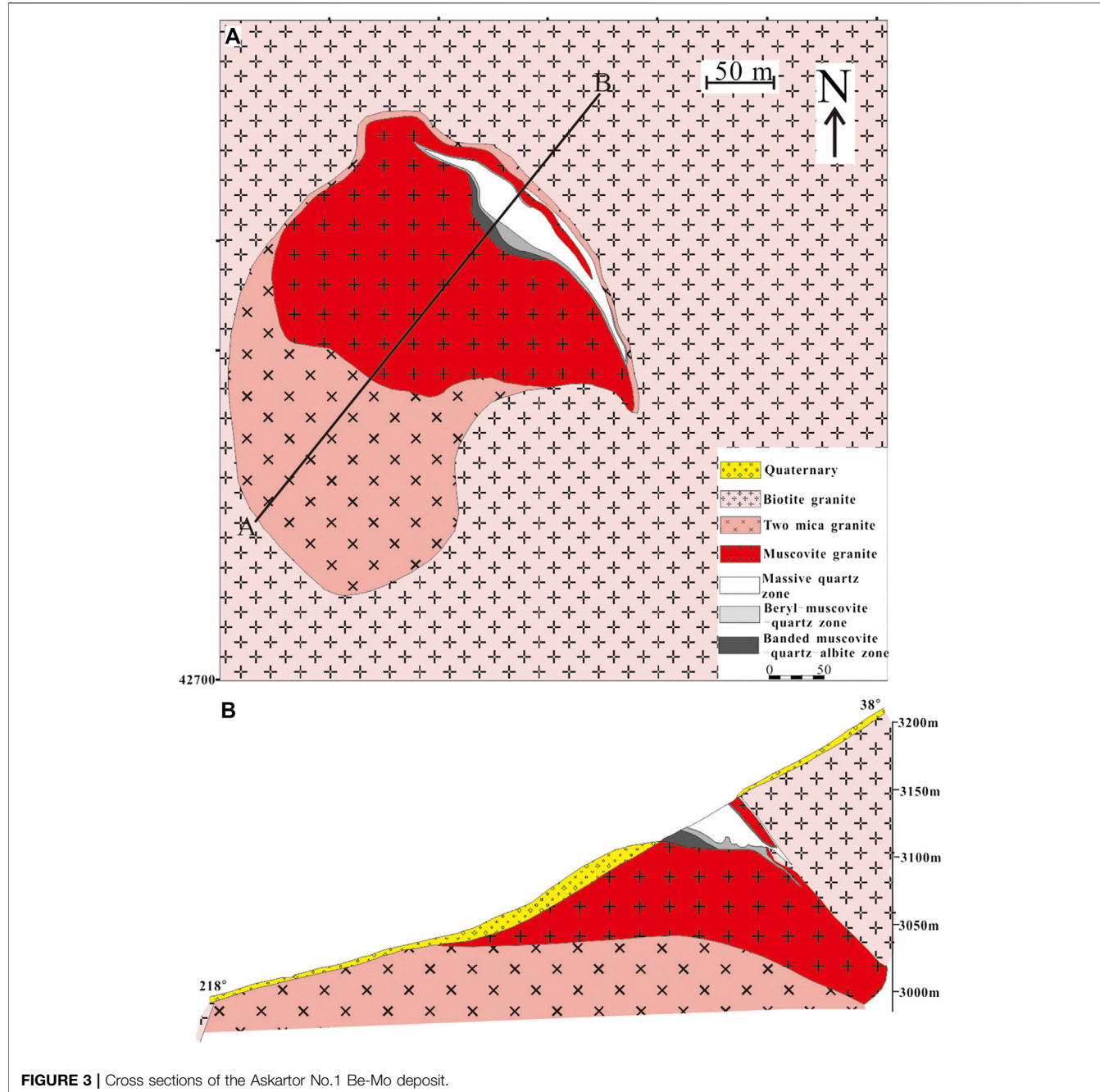


FIGURE 3 | Cross sections of the Askarto No.1 Be-Mo deposit.

- (4) Massive quartz zone (**Figure 4D**). This zone mainly consists of quartz, the colors of which are ivory, rosy, and transparency with dense block structure and the widest place of the core quartz reaches 32 m. Beryl only appears along the marginal areas, reflecting a weak Be-mineralization. There is pyrite, blende, bismuthinite, nesting of gypsum and barite vein in this zone, besides quartz, and the molybdenite appears in the inside of quartz vein's edge with little content.
- (5) Beryl-bearing muscovite-quartz zone (**Figure 4C**). This zone, showing circular distribution around the massive quartz with

0.1–5 m wide, is the primary Be-mineralization zone. The main mineral compositions are muscovite (20–30 vol%), quartz (10–20 vol%), beryl (3–5 vol%), and microcline (2–20 vol%). The molybdenite presents star-dotted lamellar and laminated shapes, coexisting with pyrite, bismuthinite, blende, spessartite, apatite, spodumene, and niobite.

- (6) muscovite-microcline-albite zone: This zone, which is 2–10 m thick with weak Be-mineralization, is in the top side of the deposit, contacting the biotite granitite wall-rock directly. The main mineral compositions are quartz

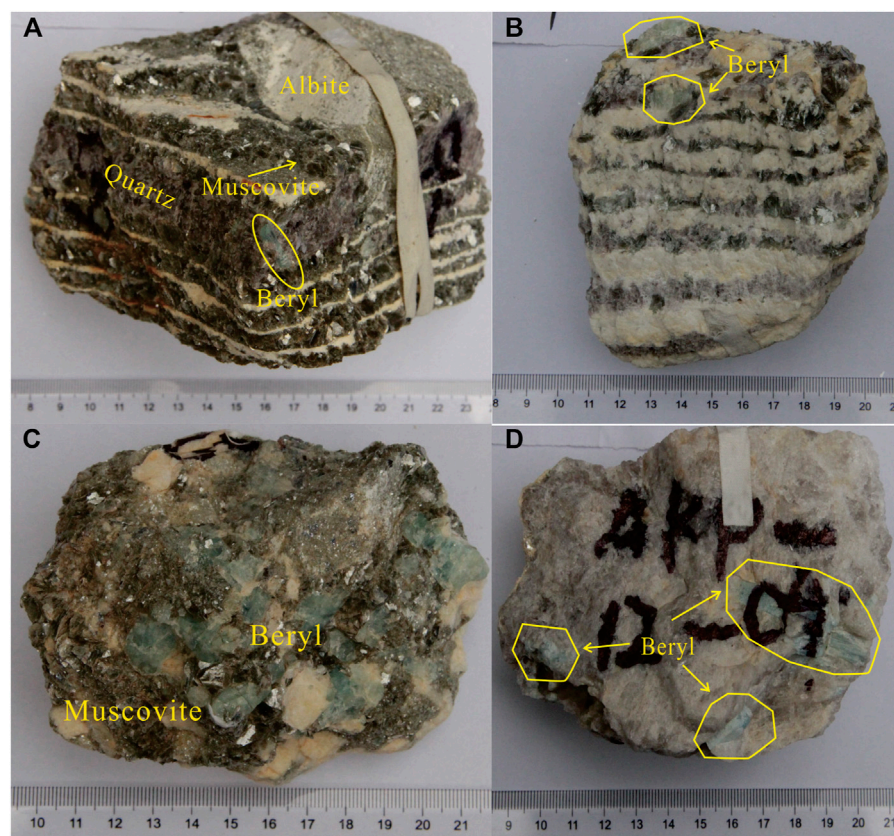


FIGURE 4 | Examples of beryl in different zones of the No.1 orebody.

(30 vol%), microcline (39 vol%), plagioclase (20 vol%), and muscovite (10 vol%), and the accessory minerals are spessartite, pyrite and molybdenite.

SAMPLES AND ANALYTICAL METHODS

Samples

Rock samples were examined by optical microscopy, and unaltered or least altered samples were selected for geochemical analysis. These samples were cleaned with deionized water, crushed, and powdered with an agate mill. Five samples were selected for zircon U-Pb dating in this study. These samples are granodiorite (sample name: AKG01, Location: N47°17'32", E90°17'38"), biotite granite (sample name: AKG02, location:N47°18'21",E90°17'39"), two-mica granite (sample name: AKG04, N47°17'33", E90°17'34"), fine-grain muscovite (sample name: AKG05, location: N47°18'19", E90°17'43"), and the banded pegmatite (sample name: AKG06, N47°18'20", E90°17'45"), respectively. Seven molybdenite samples were collected from fine-grain muscovite granite and pegmatite.

Major and Trace Elements Analysis

Major and trace elements were determined at the State Key Laboratory of Ore Deposit Geochemistry, Chinese Academy of

Sciences (SKLOGD, CAS). Major elements were analyzed by standard X-ray fluorescence (XRF). Samples were prepared as glass discs, formed by mixing 0.70 g of rock powder (dried at 110°C) with 7.0 g of lithium tetraborate for 15 min at 1,100°C in 95%P-5%Au crucibles. Analyses were performed on a PANalytical Axios PW4400 X-ray fluorescence spectrometer. The analytical precision, as determined on the Chinese National Standards GSR-1 and GSR-3, was better than 5%. Loss on ignition (LOI) was obtained using 1 g power heated to 1,100°C for 1 h.

Trace elements were analyzed with a Finnigan MAT ELEMENT magnetic sector ICP-MS. 50 mg of powdered granite sample were dissolved in a high-pressure PolyTetraFluoroEthylene (PTFE) bomb for 48 h using HF + HNO₃. Rh was used as an internal standard to monitor signal drift during counting. The USGS and Chinese National Standards BCR-1, BHVO-1, and GSR-3 were chosen for calibrating element concentrations. The discrepancy between the triplicates is less than 5% for all the elements (Qi et al., 2000).

Zircon U-Pb Dating

The zircon U-Pb dating samples were crashed, and grinded, and then separated by heavy liquid and magnetic separation methods. Zircons were picked by hand under a binocular microscope and mounted in epoxy resin. Before U-Pb dating analysis, The

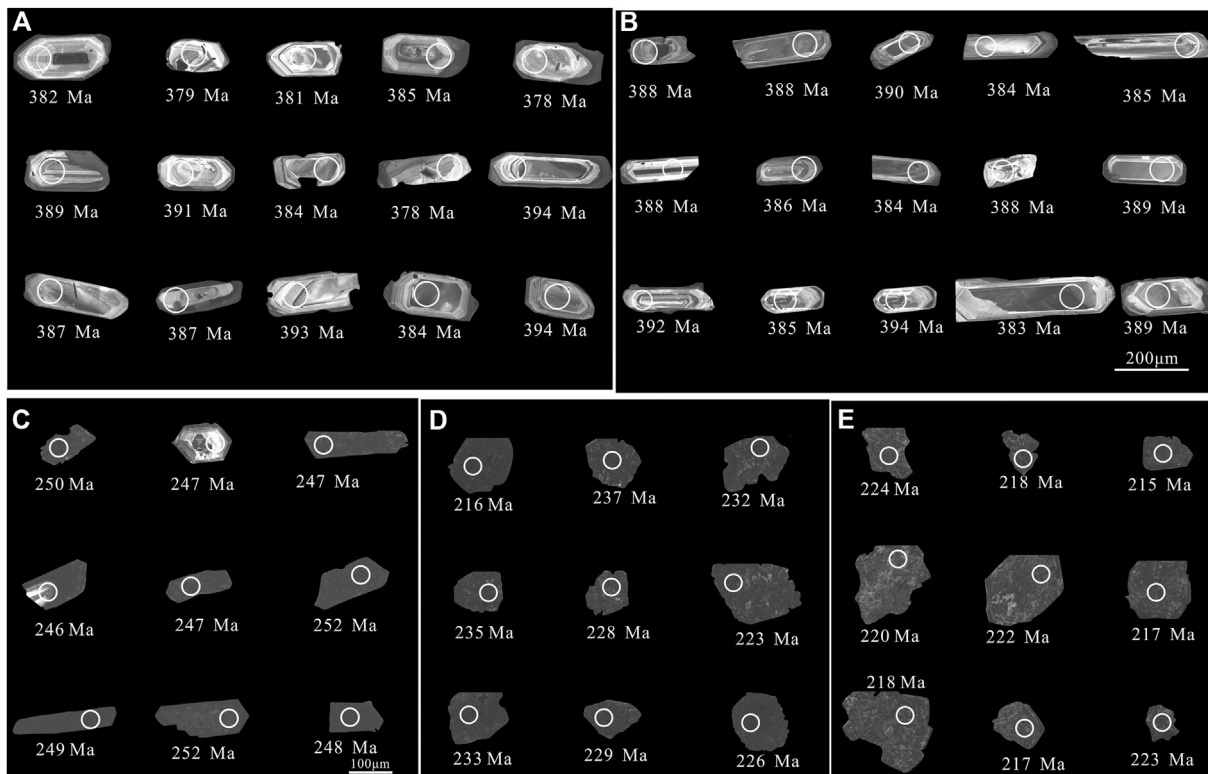


FIGURE 5 | Representative cathodoluminescence (CL) images of zircons from the different intrusions with analytical spots of the Askarto deposit. **(A)** granodiorite; **(B)** biotite granite; **(C)** two-mica granite; **(D)** muscovite granite; **(E)** pegmatite.

Cathodoluminescence (CL) images were used to assess the zircon at the Beijing zircon dating navigation technology limited company, and CL images performed at JSM6510 scanning electron microscope produced by JEOL Corporation (Japan).

Zircon U-Pb dating was done by an Elan DRC-e ICP-MS coupled with a GeoLasPro 193 nm Laser-Ablation System at SKLODG, CAS. The conditions were summarized as follows: the laser frequency was 8 Hz with an energy of 34–40 mJ; the beam diameter was 30 μm ; and the acquisition was 30 s for background and 60 s for signal. Helium was used as a carrier gas to transport the ablated materials from the laser-ablation cell to the ICP-MS torch. The external standard is Zircon 91,500, and the internal standard to calculate U, Th, and Pb concentrations of unknowns was NIST610. Glass was used as an internal standard to

Raw data were processed using the ICPMSDataCal program (Liu et al., 2008). Uncertainties of individual analyses and weighted mean ages are reported within 1σ errors; Common Pb correction used the ^{204}Pb methods of Andersen (2002). The weighted mean U-Pb ages and Concordia plots were processed using ISOPLOT software (Ludwig 2003).

Molybdenite Re-Os Dating

Seven molybdenite samples were collected from fine-grain granite and pegmatite. Molybdenite with a purity of >99% were carefully handpicked under a binocular microscope. Re-Os isotope

analyses were done at SKLODG, CAS. The analysis procedures are similar to that provided by Du et al. (2004). The ISOPLOT program (Ludwig, 2003) was used to calculate the Re-Os isochron age. The decay constant used in this calculation was $\lambda^{187}\text{Re} = 1.666 \times 10^{-11} \text{ year}^{-1}$ (Smoliar et al., 1996). Uncertainty in Re-Os model ages was 1.02% uncertainty. The uncertainty includes the ^{187}Re decay constant and uncertainty in Re and Os concentrations.

RESULTS

Zircon U-Pb Ages

Granodiorite (AKG01): the zircon grains from granodiorite are mostly light-yellow brown, transparent, and short prismatic. Their sizes are between 100 and ~300 μm . Almost all grains show clear oscillatory zoning (Figure 5A). The contents of Th and U are respectively 8–253 ppm and 172–326 ppm, and the Th/U ratios are between 0.41 and –0.85 (Table 1), indicating that these zircons are of magmatic origin. Twenty spots were selected for U-Pb analysis and these points were tightly grouped, yielding a $^{206}\text{Pb}/^{238}\text{U}$ age of 386.8 ± 2.6 Ma (MSWD = 0.54) (Figure 6A), representing the crystallization age of the pluton.

Biotite granite (AKG02): the feature of zircon grains from biotite granite is similar to that in granodiorite (Figure 5B). The contents of Th and U are 73~453 ppm and 102~646 ppm,

TABLE 1 | LA-ICPMS U-Pb data of zircons from the Askarto Be deposit.

Sample	Concentration (ppm)		Th/U	Isotopic ratio		$^{207}\text{Pb}/^{235}\text{U}$	1σ	$^{206}\text{Pb}/^{238}\text{U}$	1σ	Ages (Ma)			
	Th	U		$^{207}\text{Pb}/^{206}\text{Pb}$	1σ					$^{207}\text{Pb}/^{235}\text{U}$	1σ	$^{206}\text{Pb}/^{238}\text{U}$	1σ
AKG01.01	114	189	0.60	0.05164	0.00273	0.43061	0.02071	0.06106	0.00112	364	15	382	7
AKG01.02	116	233	0.50	0.04802	0.00216	0.40546	0.01694	0.06058	0.00096	346	12	379	6
AKG01.03	123	241	0.51	0.04695	0.00319	0.39674	0.02423	0.06084	0.00132	339	18	381	8
AKG01.04	120	222	0.54	0.05362	0.00220	0.46003	0.01773	0.06159	0.00098	384	12	385	6
AKG01.05	146	212	0.69	0.05318	0.00242	0.45116	0.02016	0.06043	0.00094	378	14	378	6
AKG01.06	160	277	0.58	0.05267	0.00247	0.45924	0.02003	0.06214	0.00102	384	14	389	6
AKG01.07	153	287	0.53	0.04878	0.00217	0.42531	0.01754	0.06251	0.00099	360	12	391	6
AKG01.08	130	222	0.58	0.05370	0.00250	0.46034	0.02064	0.06139	0.00105	384	14	384	6
AKG01.09	210	263	0.80	0.05074	0.00258	0.42444	0.02039	0.06044	0.00116	359	15	378	7
AKG01.10	112	185	0.60	0.04680	0.00249	0.41514	0.02213	0.06297	0.00120	353	16	394	7
AKG01.11	176	219	0.80	0.05420	0.00233	0.46224	0.01759	0.06187	0.00097	386	12	387	6
AKG01.12	149	326	0.46	0.04624	0.00185	0.39560	0.01460	0.06182	0.00090	338	11	387	5
AKG01.13	129	215	0.60	0.05190	0.00443	0.45338	0.03755	0.06280	0.00142	380	26	393	9
AKG01.14	112	219	0.51	0.05318	0.00301	0.45134	0.02534	0.06144	0.00135	378	18	384	8
AKG01.15	108	172	0.62	0.04750	0.00261	0.41188	0.02123	0.06300	0.00129	350	15	394	8
AKG01.16	127	308	0.41	0.04889	0.00225	0.42556	0.01818	0.06292	0.00106	360	13	393	6
AKG01.17	185	281	0.66	0.04605	0.00232	0.39918	0.01924	0.06253	0.00123	341	14	391	7
AKG01.18	124	188	0.66	0.05419	0.00273	0.47174	0.02214	0.06299	0.00116	392	15	394	7
AKG01.19	102	206	0.50	0.05198	0.00273	0.44181	0.02155	0.06250	0.00121	372	15	391	7
AKG01.20	157	249	0.63	0.05019	0.00234	0.43714	0.01953	0.06235	0.00104	368	14	390	6
AKG01.21	91	196	0.46	0.05867	0.00322	0.50699	0.02966	0.06161	0.00122	416	20	385	7
AKG01.22	184	282	0.65	0.05268	0.00212	0.45656	0.01764	0.06186	0.00095	382	12	387	6
AKG01.23	232	311	0.75	0.05240	0.00225	0.45382	0.01851	0.06205	0.00106	380	13	388	6
AKG01.24	253	297	0.85	0.05368	0.00227	0.46268	0.01870	0.06178	0.00105	386	13	386	6

Sample	Concentration (ppm)		Th/U	Isotopic ratio		$^{207}\text{Pb}/^{235}\text{U}$	1σ	$^{206}\text{Pb}/^{238}\text{U}$	1σ	Ages (Ma)			
	Th	U		$^{207}\text{Pb}/^{206}\text{Pb}$	1σ					$^{207}\text{Pb}/^{235}\text{U}$	1σ	$^{206}\text{Pb}/^{238}\text{U}$	1σ
AKG01.01	73	102	0.72	0.06418	0.00470	0.53331	0.03401	0.06208	0.00151	434	23	388	9
AKG01.02	182	337	0.54	0.05139	0.00192	0.44326	0.01562	0.06212	0.00089	373	11	388	5
AKG01.03	155	178	0.87	0.05423	0.00264	0.47109	0.02247	0.06244	0.00106	392	16	390	6
AKG01.04	109	242	0.45	0.05391	0.00258	0.45821	0.02113	0.06130	0.00090	383	15	384	5
AKG01.05	301	339	0.89	0.05167	0.00198	0.44134	0.01561	0.06155	0.00086	371	11	385	5
AKG01.06	339	363	0.93	0.05158	0.00183	0.44679	0.01488	0.06199	0.00077	375	10	388	5
AKG01.07	85	163	0.52	0.05297	0.00276	0.45214	0.02318	0.06173	0.00114	379	16	386	7
AKG01.08	82	181	0.45	0.06687	0.00316	0.57185	0.02548	0.06135	0.00113	459	16	384	7
AKG01.09	81	156	0.52	0.05182	0.00308	0.43671	0.02144	0.06210	0.00109	368	15	388	7
AKG01.10	122	207	0.59	0.05923	0.00266	0.51857	0.02309	0.06226	0.00100	424	15	389	6
AKG01.11	123	140	0.88	0.05480	0.00266	0.47020	0.02110	0.06266	0.00105	391	15	392	6
AKG01.12	453	497	0.91	0.05195	0.00153	0.45040	0.01274	0.06154	0.00078	378	9	385	5
AKG01.13	218	320	0.68	0.05196	0.00201	0.45766	0.01591	0.06303	0.00083	383	11	394	5
AKG01.14	221	420	0.53	0.04953	0.00187	0.42675	0.01517	0.06117	0.00075	361	11	383	5
AKG01.15	174	211	0.83	0.05082	0.00227	0.44076	0.01884	0.06214	0.00093	371	13	389	6
AKG01.16	273	329	0.83	0.05443	0.00199	0.47273	0.01595	0.06174	0.00080	393	11	386	5
AKG01.17	93	161	0.58	0.05384	0.00261	0.45893	0.01995	0.06235	0.00112	384	14	390	7
AKG01.18	208	328	0.63	0.05005	0.00333	0.42699	0.02773	0.06047	0.00134	361	20	379	8
AKG01.19	149	191	0.78	0.05056	0.00220	0.42830	0.01684	0.06143	0.00095	362	12	384	6
AKG01.20	251	646	0.39	0.05066	0.00148	0.44541	0.01285	0.06221	0.00074	374	9	389	4
AKG01.21	137	269	0.51	0.05317	0.00245	0.46259	0.02204	0.06240	0.00104	386	15	390	6
AKG01.22	97	182	0.53	0.05282	0.00245	0.44924	0.02006	0.06178	0.00103	377	14	386	6
AKG01.23	120	304	0.40	0.05901	0.00223	0.44341	0.01598	0.05430	0.00074	373	11	341	5
AKG01.24	343	435	0.79	0.05139	0.00176	0.41835	0.01375	0.05813	0.00073	355	10	364	4

Sample	Concentration (ppm)		Th/U	Isotopic ratio		$^{207}\text{Pb}/^{235}\text{U}$	1σ	$^{206}\text{Pb}/^{238}\text{U}$	1σ	Ages (Ma)			
	Th	U		$^{207}\text{Pb}/^{206}\text{Pb}$	1σ					$^{207}\text{Pb}/^{235}\text{U}$	1σ	$^{206}\text{Pb}/^{238}\text{U}$	1σ
AKG04.01	1,592	11,768	0.14	0.04965	0.00161	0.28534	0.00956	0.03956	0.00066	255	8	250	4
AKG04.02	1,680	12,157	0.14	0.05605	0.00187	0.32628	0.01686	0.03903	0.00123	287	13	247	8
AKG04.03	1,160	8,796	0.13	0.05658	0.00171	0.31940	0.00928	0.03910	0.00047	281	7	247	3
AKG04.04	60,118	15,458	3.89	0.06415	0.00178	0.36682	0.01357	0.03885	0.00082	317	10	246	5
AKG04.05	1,486	10,054	0.15	0.05197	0.00164	0.29778	0.01214	0.03901	0.00089	265	9	247	6

(Continued on following page)

TABLE 1 | (Continued) LA-ICPMS U-Pb data of zircons from the Askarto Be deposit.

Sample	Concentration (ppm)		Th/U	Isotopic ratio		$^{207}\text{Pb}/^{235}\text{U}$	1 σ	$^{206}\text{Pb}/^{238}\text{U}$	1 σ	Ages (Ma)			
	Th	U		$^{207}\text{Pb}/^{206}\text{Pb}$	1 σ					$^{207}\text{Pb}/^{235}\text{U}$	1 σ	$^{206}\text{Pb}/^{238}\text{U}$	1 σ
AKG04.06	772	9,875	0.08	0.05248	0.00161	0.30379	0.00996	0.03984	0.00054	269	8	252	3
AKG04.07	911	8,517	0.11	0.04810	0.00175	0.28231	0.01325	0.03942	0.00093	252	10	249	6
AKG04.08	2066	15,936	0.13	0.04504	0.00167	0.25770	0.01127	0.03992	0.00154	233	9	252	10
AKG04.09	1,507	10,554	0.14	0.05904	0.00163	0.34457	0.01288	0.03914	0.00092	301	10	248	6
AKG04.10	1,040	9,661	0.11	0.05247	0.00162	0.29513	0.00845	0.03839	0.00062	263	7	243	4
AKG04.11	617	9,999	0.06	0.04926	0.00144	0.27990	0.00824	0.03841	0.00068	251	7	243	4
AKG04.12	772	11,048	0.07	0.05071	0.00159	0.29490	0.00942	0.03907	0.00074	262	7	247	5
AKG04.13	1,561	8,696	0.18	0.05884	0.00191	0.36347	0.01064	0.04147	0.00058	315	8	262	4
AKG04.14	1,187	11,746	0.10	0.05119	0.00172	0.29746	0.01073	0.03867	0.00084	264	8	245	5
AKG04.15	482	10,083	0.05	0.05817	0.00180	0.33289	0.01242	0.03852	0.00089	292	9	244	6
AKG04.16	455	7,250	0.06	0.04612	0.00146	0.26626	0.00815	0.03939	0.00054	240	7	249	3
AKG04.17	1,080	7,121	0.15	0.05212	0.00227	0.29562	0.01312	0.03980	0.00085	263	10	252	5
Sample	Concentration (ppm)		Th/U	Isotopic ratio		$^{207}\text{Pb}/^{235}\text{U}$	1 σ	$^{206}\text{Pb}/^{238}\text{U}$	1 σ	Ages (Ma)			
	Th	U		$^{207}\text{Pb}/^{206}\text{Pb}$	1 σ					$^{207}\text{Pb}/^{235}\text{U}$	1 σ	$^{206}\text{Pb}/^{238}\text{U}$	1 σ
AKG05.01	466	8,360	0.06	0.05887	0.00396	0.27643	0.01825	0.03406	0.00046	248	15	216	3
AKG05.02	1,539	9,060	0.17	0.07022	0.00370	0.36196	0.01832	0.03739	0.00055	314	14	237	3
AKG05.03	1,385	32,709	0.04	0.05839	0.00128	0.30657	0.00648	0.03672	0.00050	272	5	232	3
AKG05.04	2,175	9,735	0.22	0.06268	0.00175	0.33484	0.00922	0.03708	0.00051	293	7	235	3
AKG05.05	1,244	7,222	0.17	0.06124	0.00281	0.30387	0.01322	0.03599	0.00053	269	10	228	3
AKG05.06	4,544	24,671	0.18	0.07573	0.00706	0.36702	0.03374	0.03515	0.00053	317	25	223	3
AKG05.07	1,453	6,478	0.22	0.05318	0.00213	0.28493	0.00935	0.03679	0.00068	255	7	233	4
AKG05.08	515	10,428	0.05	0.04876	0.00215	0.25751	0.01019	0.03616	0.00056	233	8	229	3
AKG05.09	1,048	6,806	0.15	0.05874	0.00285	0.28896	0.01335	0.03568	0.00052	258	11	226	3
AKG05.10	12,226	6,492	1.88	0.14124	0.00673	0.84036	0.04060	0.04005	0.00079	619	22	253	5
AKG05.11	4,420	8,378	0.53	0.09897	0.00833	0.54416	0.04485	0.03988	0.00069	441	29	252	4
AKG05.12	2,713	9,038	0.30	0.06395	0.00301	0.34327	0.01609	0.03606	0.00060	300	12	228	4
AKG05.13	1,671	18,199	0.09	0.05063	0.00322	0.23443	0.01453	0.03358	0.00047	214	12	213	3
AKG05.14	971	6,915	0.14	0.05554	0.00366	0.27971	0.01792	0.03652	0.00055	250	14	231	3
AKG05.15	1,130	25,526	0.04	0.05239	0.00243	0.28043	0.01268	0.03597	0.00060	251	10	228	4
AKG05.16	858	7,029	0.12	0.05235	0.00356	0.26304	0.01704	0.03645	0.00074	237	14	231	5
AKG05.17	2,947	5,148	0.57	0.07749	0.00518	0.44492	0.02590	0.03994	0.00093	374	18	252	6
AKG05.18	1,217	7,419	0.16	0.07066	0.00401	0.35344	0.01911	0.03628	0.00062	307	14	230	4
Sample	Concentration (ppm)		Th/U	Isotopic ratio		$^{207}\text{Pb}/^{235}\text{U}$	1 σ	$^{206}\text{Pb}/^{238}\text{U}$	1 σ	Ages (Ma)			
	Th	U		$^{207}\text{Pb}/^{206}\text{Pb}$	1 σ					$^{207}\text{Pb}/^{235}\text{U}$	1 σ	$^{206}\text{Pb}/^{238}\text{U}$	1 σ
AKG06.01	3,936	6,450	0.61	0.0778	0.0030	0.3940	0.0135	0.0353	0.0008	337	10	224	5
AKG06.02	3,533	6,229	0.57	0.0623	0.0024	0.3125	0.0117	0.0344	0.0007	276	9	218	4
AKG06.03	1,124	5,935	0.19	0.0456	0.0015	0.2249	0.0070	0.0339	0.0006	206	6	215	3
AKG06.04	2,150	4,780	0.45	0.0495	0.0019	0.2630	0.0098	0.0364	0.0006	237	8	230	4
AKG06.05	952	4,751	0.20	0.0474	0.0019	0.2396	0.0091	0.0348	0.0006	218	7	220	4
AKG06.06	1,603	4,578	0.35	0.0494	0.0019	0.2522	0.0093	0.0350	0.0006	228	8	222	3
AKG06.07	2,383	5,664	0.42	0.0443	0.0016	0.2227	0.0078	0.0342	0.0006	204	7	217	4
AKG06.08	796	6,841	0.12	0.0434	0.0016	0.2183	0.0076	0.0343	0.0006	201	6	218	4
AKG06.09	1867	4,985	0.37	0.0557	0.0019	0.2807	0.0096	0.0342	0.0006	251	8	217	4
AKG06.10	811	6,042	0.13	0.0391	0.0015	0.2009	0.0071	0.0352	0.0006	186	6	223	4
AKG06.11	1,594	7,267	0.22	0.0419	0.0016	0.2116	0.0075	0.0345	0.0006	195	6	219	4
AKG06.12	291	5,837	0.05	0.0432	0.0014	0.2148	0.0066	0.0341	0.0005	198	6	216	3
AKG06.13	2075	7,608	0.27	0.0395	0.0016	0.1959	0.0081	0.0340	0.0006	182	7	215	4
AKG06.14	890	5,567	0.16	0.0400	0.0015	0.2030	0.0068	0.0351	0.0007	188	6	223	4
AKG06.15	576	4,896	0.12	0.0353	0.0012	0.1814	0.0059	0.0353	0.0005	169	5	224	3
AKG06.16	372	4,870	0.08	0.0354	0.0013	0.1807	0.0063	0.0354	0.0005	169	5	224	3
AKG06.17	2,609	5,378	0.49	0.0387	0.0016	0.1992	0.0082	0.0355	0.0007	184	7	225	4
AKG06.18	1,122	5,172	0.22	0.0404	0.0014	0.2084	0.0071	0.0355	0.0005	192	6	225	3
AKG06.19	1743	6,841	0.25	0.0375	0.0012	0.1916	0.0059	0.0349	0.0005	178	5	221	3
AKG06.20	1953	4,277	0.46	0.0458	0.0026	0.2348	0.0131	0.0353	0.0008	214	11	224	5
AKG06.21	2,160	4,034	0.54	0.0474	0.0017	0.2434	0.0090	0.0348	0.0006	221	7	221	4
AKG0622	538	4,539	0.12	0.0436	0.0015	0.2278	0.0076	0.0351	0.0005	208	6	223	3
AKG0623	459	4,607	0.10	0.0449	0.0020	0.2320	0.0099	0.0350	0.0007	212	8	222	4
AKG0624	3,936	6,450	0.61	0.0778	0.0030	0.3940	0.0135	0.0353	0.0008	337	10	224	5

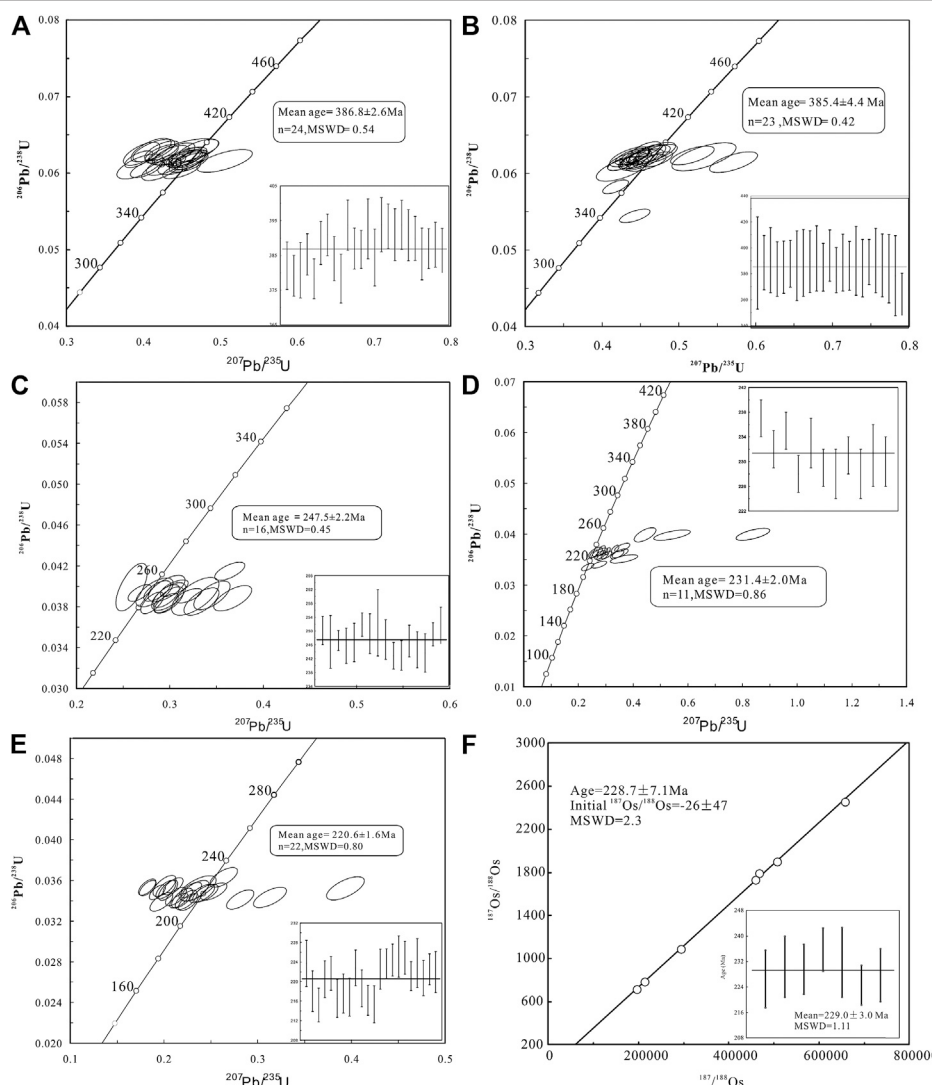


FIGURE 6 | Zircon U-Pb age of the different intrusions from the Askarto Be-Mo deposit. **(A)** granodiorite; **(B)** biotite granite; **(C)** two-mica granite; **(D)** muscovite granite; **(E)** pegmatite, and **(F)** Re-Os isochron age of molybdenites.

respectively, and the Th/U ratios ranged from 0.39 to 0.93. Twenty-three yielded concordant $^{206}\text{Pb}/^{238}\text{U}$ ages with a weighted mean age of 385.8 ± 4.4 Ma (MSWD = 0.42, $n = 23$) (**Figure 6B**), representing the crystallization age of this rock. One point showed a younger age of 341 ± 5 Ma (**Table 1**, AKG02.23), which may be affected by minor Pb loss.

Two-mica granite (AKG04): The zircon grains separated from two-mica granite are mostly brown and opaque, and varying in size of 80–220 μm , with euhedral habit featuring tetragonal dipyramid \pm prism. They show weak and intense luminescences in CL photos, with reservation of primary oscillatory zone in some zircons (**Figure 5C**). The CL features indicate that the zircons have suffered from low degree of recrystallization induced by metamictization due to high contents of U (7,121~15936 ppm) and Th (mostly fall in range of 455~2066 ppm) and fluid alteration after crystallization from

melting. The zircons mostly have low Th/U ratios of 0.1–0.2. Seventeen analytical points were conducted on the zircons with legible oscillatory zones, and sixteen of them yielded consistent and concordant $^{206}\text{Pb}/^{238}\text{U}$ ages with a weighted mean age of 247.5 ± 2.2 Ma (MSWD = 0.45) (**Figure 6C**), which represents the crystallization time of the muscovite granite. The rest one analytical point yielded an older $^{206}\text{Pb}/^{238}\text{U}$ age of 262 ± 3.6 Ma (**Table 1**, AKG04.16), which may reflect the incorporation of common lead after crystallization.

Fine-grain muscovite granite (AKG05): Zircons from fine-grain muscovite granite generally exhibit euhedral tetragonal-dipyramid or stubby tetragonal prism shapes and range from 80 to 180 μm in size. Most of them are opaque and brown to dark brown in color, with weak oscillatory zoning structure (**Figure 5D**). Th and U contents of the zircon grain are 466–4,544 ppm and 5,148–32,709 ppm, respectively, with Th/U

TABLE 2 | The whole-rock compositions of different intrusions from Askartor Be deposit.

Rock type	Sample	Two-mica granite						Muscovite granite granite	AKG-12-04C
		AKG-12-04K-A	AKG-12-03A-A	AKG-12-03B-D	AKG-12-03C	AKG-12-03D	AKG-12-03E		
SiO ₂	74.77	73.87	73.37	73.10	73.05	74.25	75.06	74.58	74.21
TiO ₂	0.07	0.09	0.24	0.19	0.20	0.16	0.09	0.05	0.15
Al ₂ O ₃	14.47	14.38	13.43	14.86	14.04	14.16	14.06	14.16	14.40
FeO/FeO _T	0.76	0.83	0.92	1.11	1.14	0.97	0.71	0.49	0.90
MnO	0.03	0.04	0.04	0.05	0.04	0.05	0.02	0.02	0.02
MgO	0.17	0.20	0.23	0.27	0.29	0.22	0.17	0.12	0.19
CaO	0.36	0.53	0.60	0.74	0.76	0.42	0.48	0.58	0.56
Na ₂ O	4.28	4.21	3.47	3.72	3.06	3.41	4.06	4.58	3.64
K ₂ O	3.89	4.11	3.99	4.39	4.12	4.01	4.13	3.83	4.46
P ₂ O ₅	0.17	0.19	0.16	0.18	0.19	0.18	0.17	0.14	0.18
LOI	0.87	0.94	1.32	0.54	1.23	1.63	0.72	0.66	0.97
Total	99.84	99.39	99.91	99.15	98.12	99.45	99.67	99.21	99.69
A/CNK	1.22	1.17	1.21	1.22	1.29	1.32	1.17	1.11	1.24
Li	107.0	148.0	183.0	211.0	236.0	100.0	75.1	151.0	97.8
Be	12.6	12.8	12.6	21.7	15.3	9.1	9.0	12.7	13.8
Re	345.0	401.0	386.0	343.0	345.0	350.0	309.0	271.0	364.0
Sr	21.7	32.8	46.4	52.8	47.8	43.2	19.2	14.7	24.1
Y	6.8	5.9	8.0	8.6	9.1	5.6	4.0	3.4	5.8
Zr	59.8	67.4	83.9	106.0	119.0	92.3	54.0	33.3	83.8
Nb	19.7	20.3	17.6	18.9	19.9	21.2	14.4	12.1	17.2
Ba	58.4	88.7	135.0	131.0	104.0	115.0	26.2	15.2	50.7
La	4.86	11.60	13.70	23.50	19.90	12.90	8.57	5.76	10.90
Ce	15.00	26.20	28.80	50.50	41.90	34.00	19.30	11.00	23.10
Pr	1.35	3.08	3.52	6.23	5.27	3.39	2.22	1.49	2.97
Nd	5.31	11.10	13.40	23.10	19.60	12.80	8.08	5.43	11.30
Sm	1.09	1.89	2.28	3.89	3.61	2.14	1.43	1.04	2.05
Eu	0.13	0.25	0.32	0.41	0.36	0.25	0.16	0.11	0.20
Gd	0.89	1.19	1.55	2.35	2.20	1.41	0.98	0.58	1.30
Tb	0.17	0.19	0.23	0.35	0.33	0.21	0.14	0.10	0.21
Dy	1.04	0.95	1.20	1.55	1.54	1.00	0.64	0.52	2.10
Ho	0.22	0.18	0.24	0.28	0.28	0.18	0.12	0.10	0.17
Er	0.69	0.54	0.82	0.82	0.85	0.54	0.37	0.33	0.56
Tm	0.12	0.09	0.15	0.12	0.12	0.08	0.05	0.05	0.08
Yb	0.78	0.67	1.23	0.80	0.83	0.60	0.38	0.35	0.54
Lu	0.13	0.10	0.19	0.11	0.12	0.10	0.05	0.05	0.13
Hf	2.3	2.3	2.6	3.0	3.6	2.9	1.9	1.3	2.8
Ta	3.3	2.1	2.6	2.6	3.1	2.1	1.7	1.5	3.0
Th	8.0	11.1	12.2	21.1	19.8	13.6	8.5	4.8	15.3
U	1.8	4.6	1.9	4.1	11.3	2.1	4.9	0.9	13.3
Nb/Ta	6.0	9.8	6.8	7.2	6.3	9.9	8.2	8.0	5.7
Zr/Hf	26.3	30.0	32.0	34.9	32.8	31.4	28.9	26.0	30.0
Y/Hf	30.5	32.7	33.4	31.2	32.6	30.2	34.1	34.5	33.6
Sr/Er	172.8	131.7	143.8	128.2	131.4	170.8	123.7	128.1	121.5
ΣREE	31.77	58.03	67.63	113.98	96.91	69.40	42.48	26.92	54.44
δEu	0.39	0.50	0.52	0.41	0.39	0.44	0.40	0.45	0.37
8Ge	1.40	1.05	1.00	0.99	1.00	0.98	1.23	1.06	0.90
TE3.4	1.03	1.04	1.02	1.02	1.00	0.99	0.98	1.03	1.06
Muscovite granite									
Rock type sample	AKG-12-04G	AKG-12-04J	AKG-12-04M	AKG-12-04N	AKG-12-04L	AKG-12-04O	AKG-12-04B	AKG-12-04H	AKG-12-04R-A
SiO ₂	74.33	74.85	75.41	74.87	74.86	74.04	74.04	72.64	75.05
TiO ₂	0.06	0.05	0.04	0.03	0.04	0.03	0.01	0.01	0.01
Al ₂ O ₃	14.70	14.81	13.78	14.61	14.51	15.00	15.34	14.15	15.38
FeO/FeO _T	0.51	0.42	0.27	0.33	0.41	0.17	0.43	0.22	0.11
MnO	0.02	0.01	0.02	0.02	0.02	0.02	0.04	0.04	0.04
MgO	0.09	0.04	0.03	0.02	0.02	0.02	0.04	0.03	0.00

(Continued on following page)

TABLE 2 | (Continued) The whole-rock compositions of different intrusions from Askartor Be deposit.

Rock type	Sample	Two-mica granite						Muscovite granite		AKG-12-04C	
		AKG-12-04K-A	AKG-12-05A-A	AKG-12-05B-D	AKG-12-05C	AKG-12-05D	AKG-12-05E	AKG-12-04D-A	AKG-12-04E-A	AKG-12-04F	
CaO	0.19	0.26	0.25	0.16	0.25	0.22	0.07	0.33	0.15	0.09	0.09
Na ₂ O	4.04	4.36	3.77	4.49	4.53	4.76	5.51	5.41	5.96	6.03	4.52
K ₂ O	4.47	4.14	4.80	3.87	3.77	3.96	3.90	2.92	4.39	3.07	3.38
P2O ₅	0.11	0.09	0.11	0.11	0.11	0.14	0.11	0.19	0.15	0.13	0.10
Li ₂ O	0.55	0.74	1.00	0.91	1.00	0.84	1.04	0.69	0.49	0.89	0.75
Total	99.08	99.77	99.46	99.42	99.47	99.51	98.80	99.26	99.31	99.69	99.72
A/CNK	1.24	1.22	1.16	1.23	1.21	1.20	1.14	1.12	1.08	1.13	1.37
Li	70.8	66.2	45.5	56.5	45.5	37.5	30.4	23.5	23.7	29.7	36.3
Be	10.0	10.5	9.7	10.3	11.0	8.0	200.6	311.9	300.8	355.9	175.2
Rb	359.0	323.0	349.0	344.0	317.0	431.0	448.0	587.0	454.0	318.0	385.0
Sr	34.6	6.8	7.7	5.0	15.0	8.3	14.6	21.0	21.1	12.4	5.9
Y	2.8	2.3	2.9	4.4	3.0	3.9	5.3	5.8	5.6	5.6	2.5
Zr	15.1	18.2	15.5	33.2	14.6	23.0	26.7	23.0	20.8	21.4	22.5
Nb	17.5	14.4	8.6	13.9	15.5	21.4	98.7	96.7	110.0	105.0	80.6
Ba	6.6	7.2	5.2	3.1	4.0	13.6	15.4	32.3	30.6	19.5	5.9
La	1.35	1.82	1.89	1.79	1.05	1.18	0.41	0.68	1.04	0.90	0.58
Ce	2.93	3.54	3.74	3.36	2.26	2.20	0.79	1.56	2.05	1.51	1.16
Pr	0.35	0.43	0.49	0.42	0.24	0.27	0.10	0.19	0.21	0.11	0.13
Nd	1.20	1.45	1.58	1.41	0.70	0.64	0.32	0.68	0.66	0.40	0.41
Sm	0.32	0.32	0.38	0.37	0.21	0.23	0.08	0.16	0.20	0.10	0.10
Eu	0.05	0.04	0.03	0.04	0.04	0.03	0.01	0.02	0.02	0.03	0.02
Gd	0.25	0.26	0.26	0.31	0.18	0.20	0.09	0.18	0.15	0.12	0.10
Tb	0.06	0.05	0.05	0.08	0.04	0.05	0.04	0.06	0.05	0.06	0.03
Dy	0.35	0.30	0.37	0.58	0.29	0.39	0.40	0.53	0.44	0.53	0.21
Ho	0.07	0.07	0.07	0.12	0.07	0.08	0.12	0.14	0.09	0.12	0.05
Er	0.22	0.21	0.26	0.45	0.26	0.32	0.36	0.39	0.38	0.47	0.22
Tm	0.04	0.04	0.04	0.09	0.06	0.07	0.09	0.12	0.08	0.08	0.06
Yb	0.27	0.30	0.33	0.66	0.46	0.59	0.77	0.88	0.70	0.81	0.59
Lu	0.04	0.04	0.05	0.11	0.07	0.09	0.11	0.11	0.11	0.11	0.10
Hf	0.8	0.9	0.7	1.7	0.8	1.5	4.3	4.1	3.5	4.0	1.6
Ta	3.2	2.2	1.3	2.0	2.4	3.4	61.4	116.0	98.2	78.8	51.2
Th	2.8	2.7	2.1	2.9	1.5	1.6	3.4	3.9	4.8	5.4	0.8
U	2.1	8.0	1.5	3.2	1.4	2.0	18.4	16.6	10.8	5.8	2.3
Nb/Ta	5.4	6.6	6.8	6.9	6.5	6.2	1.6	0.8	1.1	1.3	1.6
Zr/Hf	18.5	19.3	21.8	19.2	17.4	15.1	6.2	5.6	5.9	5.3	14.2
Y/Ho	38.6	34.7	40.0	35.8	42.9	48.9	45.4	42.6	60.3	45.5	54.2
Sr/Eu	666.7	168.9	144.4	167.9	419.4	261.3	1,440.6	900.2	841.5	563.1	370.7
ΣREE	7.50	8.87	9.56	9.76	5.93	6.52	3.86	5.70	6.20	5.33	3.75
ΣEu	0.56	0.49	0.52	0.27	0.56	0.44	0.37	0.42	0.43	0.61	0.48
ΣCe	1.03	0.96	0.94	0.93	1.08	0.94	0.94	1.04	1.06	1.16	1.00
TE34	0.38	0.28	0.32	0.33	0.31	0.31	0.30	0.38	0.31	0.18	0.28

ratios in the range of 0.06–0.30 (**Table 1**). Seventeen spots were selected from domains of homogenous composition and clear oscillatory zoning for U-Pb analysis. Of these, eleven yield an age population with a weighted mean $^{206}\text{Pb}/^{238}\text{U}$ age of 231.4 ± 2.0 Ma (**Figure 6D**), representing the crystallization age of zircons. Four spots yield younger ages (213–226), deviating from the concordia due to a small amount of Pb loss or inclusions. The remaining spot yields an older age of 252 Ma, most likely representing the formation age of xenocrysts.

Pegmatite (AKG06): The zircon grains from the banded pegmatite collected for U-Pb dating are similar to those from sample AKG05 in color, transparency, crystal habit, and grain size. Some zircons show metasomatic relict textures in CL photos, and are characterized by microtaxitic mantle-core with nonuniform luminescences and relict rim with uniform luminescence, indicating evident metasomatic alteration after crystallization. The primary zircon domains are featured by weak and uniform luminescences, embayed texture, and regular or irregular shapes, and are enclosed by spongy domains (**Figure 5E**). All these features suggest that the zircons have suffered from metamictization, metasomatism, and recrystallization to different extents. The zircons have Th and U contents of 291~3,936 ppm and 4,034~7,608 ppm, respectively, with varying Th/U ratios from 0.05 to 0.61. Twenty-four analytical points were conducted on the primary zircon domains and twenty-two of them yielded consistent and concordant $^{206}\text{Pb}/^{238}\text{U}$ ages with a weighted mean age of 220.6 ± 1.6 Ma (MSWD = 0.80) (**Figure 6E**), which represents the crystallization time of the pegmatite. The other two points yielded inconcordant ages, indicating the incorporation of common lead after crystallization or influence of mineral inclusion in zircon.

Molybdenite Re-Os Ages

The Re-Os isotope results of the 7 molybdenite samples are shown in **Table 2**. The Re content of molybdenite is between 38 and 56 ppm with an average of 47 ppm. The Re-Os model ages of 7 molybdenite samples range from 224.6 ± 3.1 to 235 ± 3.4 Ma, with a weighted mean age of 229.0 ± 3.0 Ma (**Table 3**). ISOPLOT software was used to calculate the isochron age for the seven data points, and derived an isochron age of 228.7 ± 7.1 Ma (**Figure 6D**). The isochron age represents the time of molybdenite crystallization.

Geochemical Characteristic

The two-mica granite, muscovite granite, and beryl-bearing muscovite granite are rich in SiO_2 (71.92–75.41 wt%), Al_2O_3 (13.43–15.98 wt%), and total alkali $\text{Na}_2\text{O} + \text{K}_2\text{O}$ (7.18–10.35 wt %), poor in CaO (0.07–0.76 wt%), TFe_2O_3 (0.11–1.14 wt%), and TiO_2 (0.01–0.25 wt%) (**Table 2**). In the TAS diagram, all the samples fall in the granite area (**Figure 7A**); on the $\text{K}_2\text{O}-\text{SiO}_2$ diagram, most of the samples fall in the range of high-k calc alkaline series (**Figure 7B**); the A/CNK index varies from 1.1 to 1.3 (**Figure 7C**), with strong peraluminous characteristics. Compared with the former two, beryl-bearing muscovite granite has higher $\text{Na}_2\text{O}/\text{K}_2\text{O}$ ratio ($\text{Na}_2\text{O}/\text{K}_2\text{O} = 1.2\text{--}2.0$). The REE content decreases gradually from two mica granite

($\sum\text{REE} = 27\text{--}114.0$ ppm), medium fine-grained muscovite granite ($\sum\text{REE} = 4\text{--}10$ ppm) to beryl-bearing muscovite granite ($\sum\text{REE} = 4\text{--}6$ ppm); The rock samples all have negative Eu anomalies ($\delta\text{Eu} = 0.27\text{--}0.61$). The Lanthanide tetrad effects in the REE patterns are observed in muscovite granite. The degrees of the tetrad effects ($\text{TE}_{3,4}$) in the muscovite and beryl-bearing muscovite granite are in the range of 1.08~1.19 and 1.24~1.34, respectively, (**Table 2**; **Figures 8A,B**).

In the normalized spider web diagram of trace element primitive mantle, all of the rock samples show enrichment of large ion lithophile elements, and have obvious negative anomalies of Ba, Sr, and Ti (**Figures 8C,D**).

DISCUSSION

The Formation age of Be Deposit in Altay

The zircon U-Pb age of pegmatoid orebody is 220.6 ± 1.6 Ma which coincides with the molybdenite Re-Os isochron age of 228.7 ± 7.1 . This age is slightly younger than that of muscovite granite (231.4 ± 2.0 Ma). The zircon U-Pb age of the Askartor Be-Mo deposit obtained in this paper is consistent with that of the previous study (Wang et al., 2015) (**Table 4**).

Recent studies have revealed that the geodynamic change in the Triassic period played a key role in the formation of rare-metal deposits in Altay, NW China. These deposits include (see **Table 4**): Koktokay No.3 pegmatite-type Li-Be-Ta-Nb-Cs deposit (220–209 Ma, Chen, 2011; Wang et al., 2007); Koktokay No.1 and Koktokay No.11 pegmatite-type Li-Be-Ta-Nb (208 and 212 Ma, respectively, Ren et al., 2011); Kelumute No.112 pegmatite-type Li-Be-Nb-Ta deposit (238–211 Ma, Lv et al., 2012), and Fuhai No.11 pegmatite-type Li-Be-Nb-Ta deposit (203 Ma, Lv et al., 2012). Some medium-scale Be-Nb-Ta deposits and small-scale pegmatite-type Be in Altay, such as Kalaerqisi, Qiebielin-xiaokalasu, and Jiamanhaba pegmatites were dated at 250–209 Ma (Ren et al., 2011; Ma et al., 2015).

Thus, the formation of Askartor Be-Mo deposit is not an accidental metallogenic event, but is representative of the Triassic rare metal metallogenic event in Altay.

The Genesis of Askartor Be-Mo Deposit

The two-mica granite, muscovite granite, beryl-bearing muscovite granite, and pegmatoid shell have a close spatial and temporal relationship, with similar zircon Hf isotopic composition (Wang et al., 2015). These features indicate that these rocks may be the products of the same magmatic system at different evolution stages.

As shown in **Figure 9**, although the beryl-bearing muscovite granite has higher Na_2O content and $\text{Na}_2\text{O}/\text{K}_2\text{O}$ ratio, the evolutionary relationship among the major elements of the three types of granites is not obvious. The proportion of rock-forming minerals (such as quartz and feldspars) of the three types of granites is basically the same, which is close to the proportion of the minimum composition, $\text{Ab}_{37}\text{Ms}_{10}\text{Or}_{20}\text{Qtz}$ (Icenhower and London, 1995). Therefore, these rocks can be the products of

TABLE 3 | Re-Os data of molybdenite from the Arskartor Be deposit.

Sample	Re (ppm)		^{187}Re (ppm)		^{187}Os (ppb)		Ages (Ma)	
	Measured	1 σ	Measured	1 σ	Measured	1 σ	Measured	1 σ
QHA12-02	49.7	2.3	31.1	1.4	117.1	2.3	226.5	4.5
QHA12-03	43.3	2.0	27.1	1.3	103.8	2.2	230.4	4.8
QHA12-04	45.7	0.7	28.6	0.4	109.3	1.9	229.6	3.9
QHA12-05	38.3	0.7	24.0	0.4	93.90	1.4	235.7	3.4
QHA12-07	56.4	0.7	35.3	0.4	136.2	3.2	231.8	5.5
QHA12-08	46.8	0.8	29.3	0.5	109.4	1.5	224.6	3.1
QHA12-10	50.9	1.5	31.7	1.0	120.1	2.2	227.8	4.2

model continuous fractional crystallization in the same magmatic systems.

One consequence of Goldschmidt's Rule is that isovalent trace elements of equal or very similar ionic radii should remain tightly coupled in geological processes. If, however, in certain geological systems other properties become important, this coherency is likely to break down. In octahedral coordination, Y^{3+} , Ho^{3+} , Zr^{4+} , Hf^{4+} , Nb^{5+} , and Ta^{5+} show effective ionic radii of 1.04, 1.04, 0.86, 0.85, 0.78, and 0.78, respectively, (Shannon, 1976). Hence, the element pairs Y-Ho, Zr-Hf, and Nb-Ta are geochemical twin pairs. The fractionation of these trace element pairs occurred in muscovite granites, with the increase degree of the tetrad effect (**Figure 10**). The fractionation of isovalent trace element and the lanthanide tetrad are known to indicate magmatic-hydrothermal transition environments (e.g., Bau, 1996; Irber, 1999; Monecke et al., 2002; Monecke et al., 2007; Ballouard et al., 2016). The characteristics of trace elements indicate that muscovite granites have undergone self-metasomatism. This self-metasomatism refers to the reaction between the fluid, excluding from the granitic magma, and incompletely crystallized granite.

Based on the partition coefficients of Be and the results of this study, we preliminarily established the mineralization model of Askartor Be-Mo deposit (**Figure 11**). The model is mainly established on the basis of the Rayleigh fractional crystallization equation:

$$C^{RL} = C^L f^{D^S-1} \quad (1)$$

$$\bar{C}^S = C^L \times \frac{(1-f^{D^S})}{1-f} \quad (2)$$

C^L : concentration of Be in initial magma.

C^{RL} : instant concentration of Be in residual magma.

C^S : average concentration of Be in crystalline solid.

D^S : The total partition coefficient of Be

f : ratio of residual magma to initial magma.

The inclusion data show that the emplacement pressure and temperature of the initial magma of the Askartor Be-Mo deposit are 500 MPa and $750 \pm 50^\circ\text{C}$ (Ding, 2016). At these temperature and pressure conditions, the minimum and maximum water contents in the initial magma are 4 wt% and 10 wt%, respectively, (Holtz et al., 2001). When we assume that the water content of the initial is 4%, according to the balance calculation: $4 \text{ wt\%} = (1-f) \times 0 \text{ wt\%} + f \times 10 \text{ wt\%}$

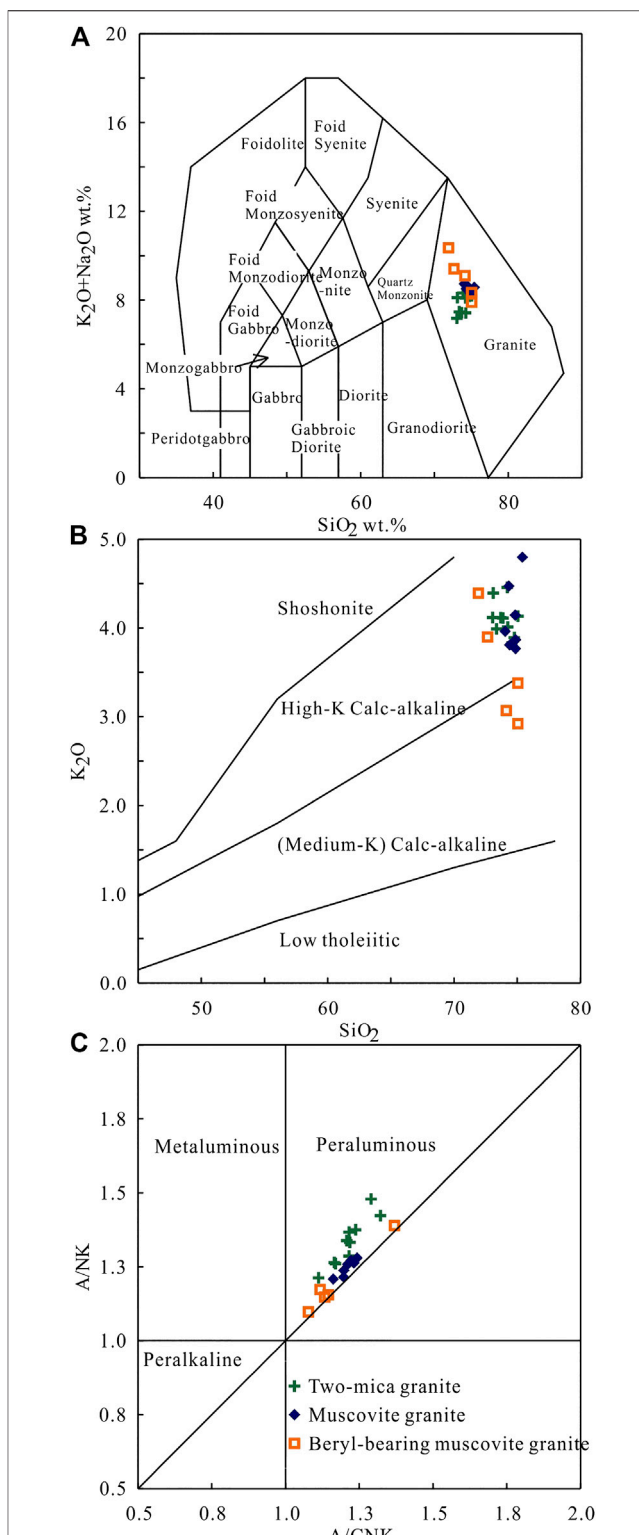


FIGURE 7 | Geochemical characterization of the different intrusions from the Askartor Be-Mo deposit. **(A)** SiO_2 vs. $\text{Na}_2\text{O} + \text{K}_2\text{O}$ [after Middlemost (1994)]; **(B)** SiO_2 vs. K_2O [after Rickwood (1989)]; **(C)** A/CNK vs. A/NK [after Maniar and Piccoli (1989)].

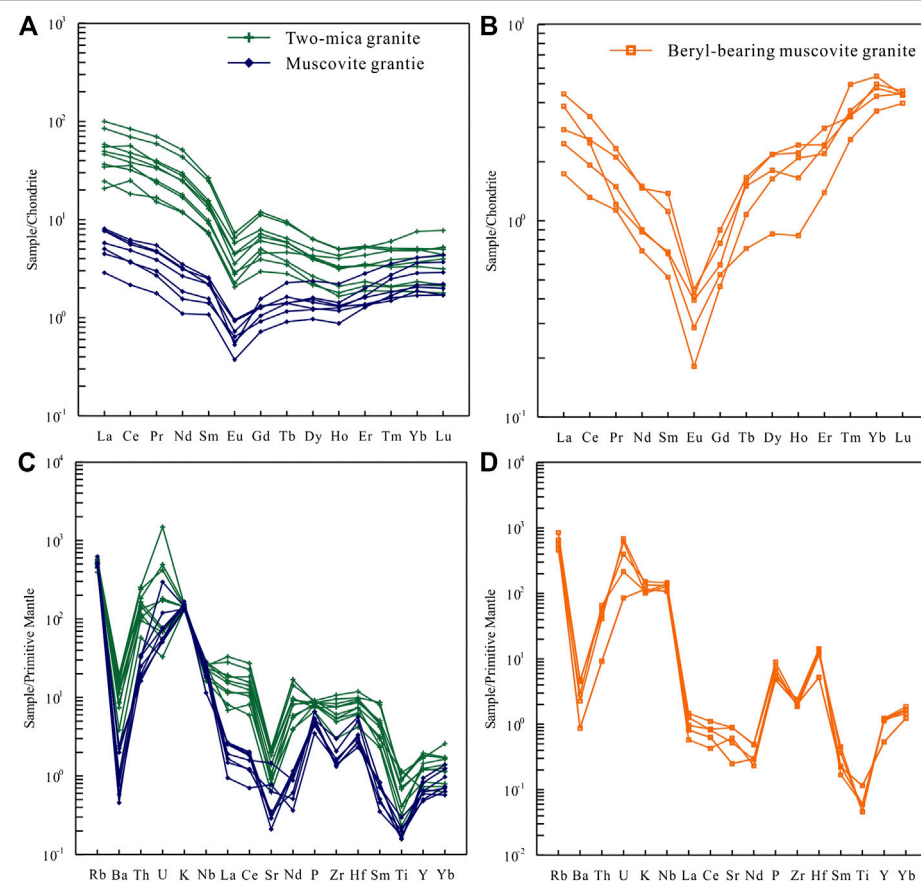


FIGURE 8 | The Chondrite-normalized rare earth element (REE) patterns and Primitive-mantle-normalized spider diagram of the different intrusions from the Askartor Be-Mo deposit. **(A, C)** two-mica and muscovite granite; **(B, D)** beryl-bearing muscovite granite. Symbols are as in **Figure 7**. Chondrite and primitive-mantle values are from Sun and McDonough (1989).

TABLE 4 | Age of rare metal deposit in the Chinese Altay orogenic belt.

Location	Deposit type	Deposit name	Mineralization type	Age (Ma)	Dating method	Reference
Koktokay	Pegmatite	KKT03	Li-Be-Ta-Nb-Cs	220–209	U-Pb	Chen (2011)
	Pegmatite	KKT01	Li-Be-Ta-Nb	208.1 ± 0.8	U-Pb	Wang et al. (2007)
	Pegmatite	KKT11	Li-Be-Ta-Nb	212.7 ± 2.5	U-Pb	Ren et al. (2011)
	Pegmatite	FH11	Be-Ta-Nb	202.9 ± 0.8	U-Pb	Ren et al. (2011)
Kalaerqisi	Pegmatite	KLMT112	Li-Be-Ta-Nb	238–211	U-Pb	Lv et al. (2012)
	Pegmatite	KKLG650	Li-Be-Ta-Nb	228–211	U-Pb	Ren et al. (2011)
	Pegmatite	JMK02	Li-Be-Ta-Nb	212.2 ± 1.7	U-Pb	Ma et al. (2015)
	Pegmatite	QK02	Be-Ta-Nb	206.8 ± 1.6	U-Pb	Ren et al. (2011)
Qiebielin-xiaokalasu	Pegmatite	FH08	Be-Ta-Nb	244.3 ± 1.1	U-Pb	
	Pegmatite	ALT01	Be-Ta-Nb	246.8 ± 1.2	U-Pb	
	Pegmatite	BRJ10	Be	249.7 ± 0.7	U-Pb	
	Pegmatite	BRJ07	Be	240.5 ± 1.4	U-Pb	
Jiamanhaba Askartor	Pegmatite	HB07	Be	237.5 ± 2.6	U-Pb	
	Granite ± pegmatite	Askartor	Be-Mo	220.6 ± 1.6	U-Pb	This study
				218.2 ± 3.9	U-Pb	Wang et al. (2015)
				228.7 ± 7.1	Re-Os	This study
				218.6 ± 1.3	Re-Os	Wang et al. (2015)

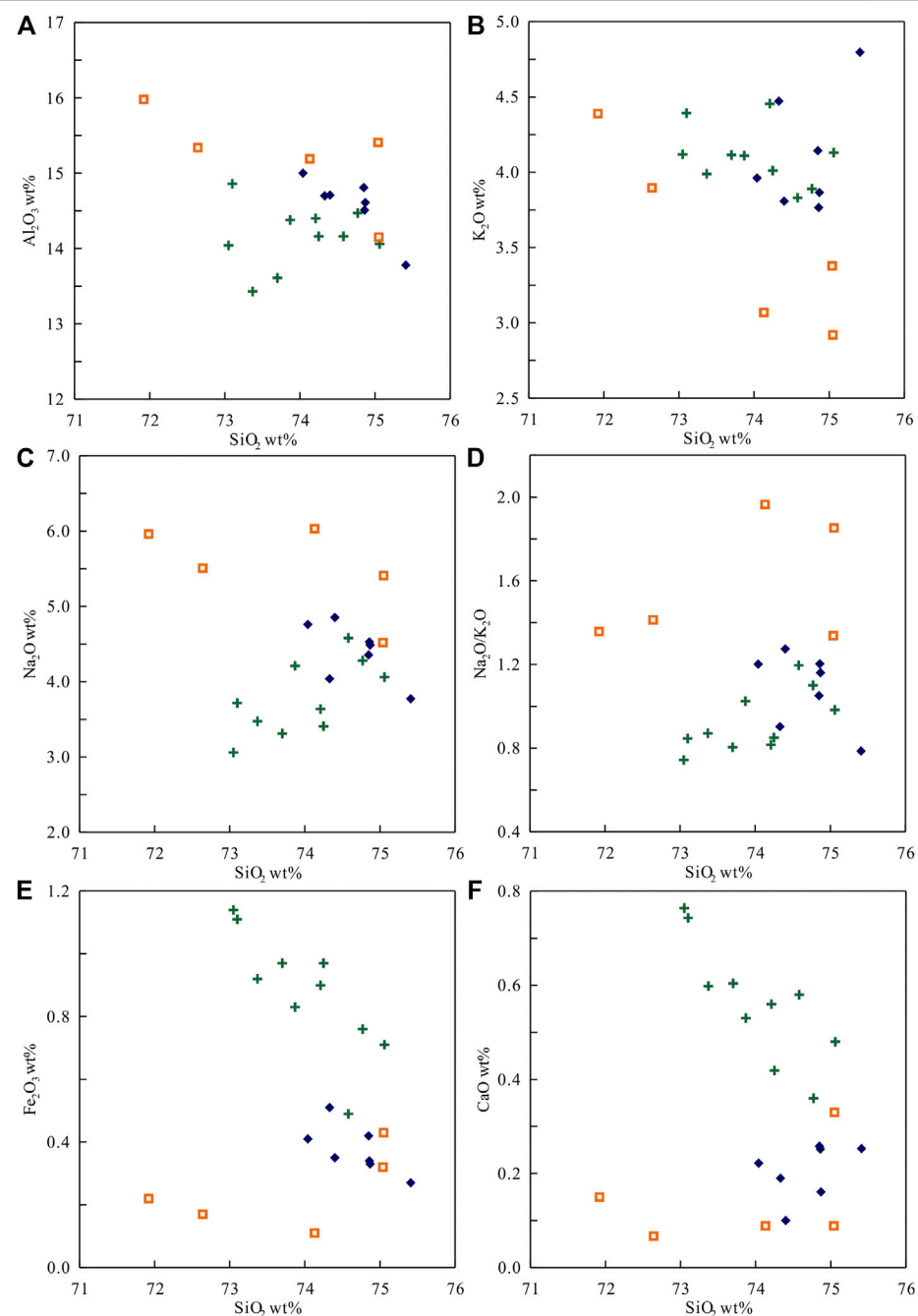
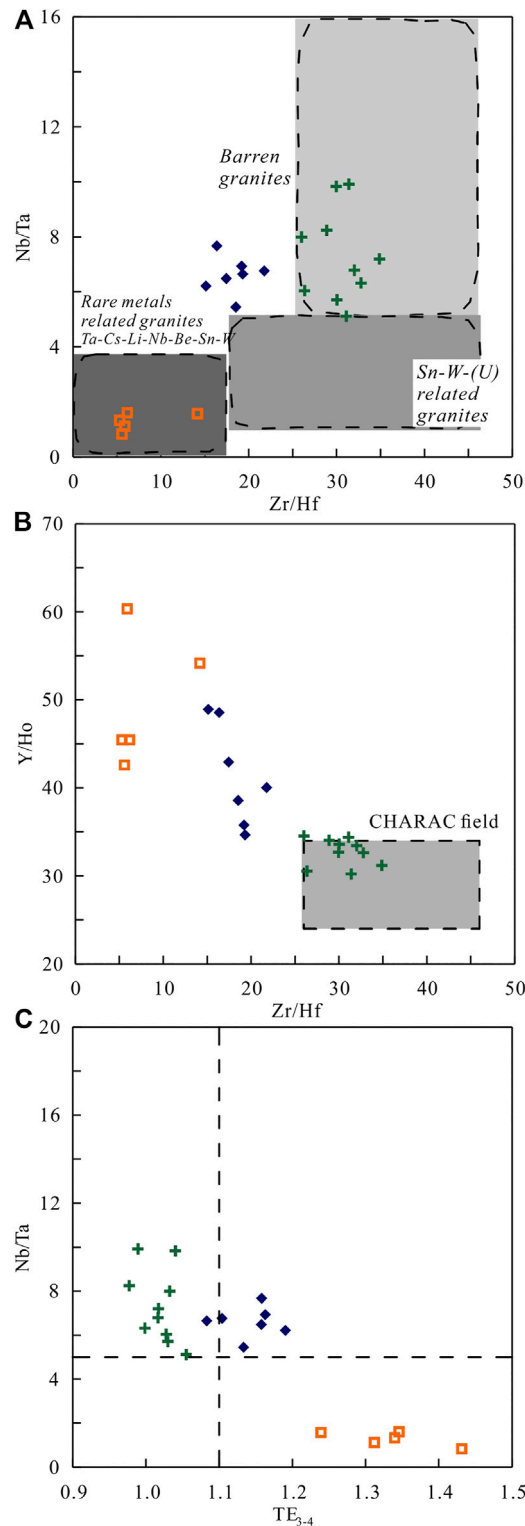


FIGURE 9 | Bivariate plots of the oxides Al_2O_3 , K_2O , Na_2O , Fe_2O_3 , CaO , and $\text{Na}_2\text{O}/\text{K}_2\text{O}$ ratios vs. SiO_2 of the different intrusions from the Askartor Be-Mo deposit.

%, when the water content in magma will reach 10 wt%, the f equals to 0.4. Even if we consider hydrous minerals like mica, because the content of mica is low, it has little effect on the results. Trace element data show that the two-mica granite should be the product of pure magmatic crystallization, so at this stage, the fractional degree of initial magma will not exceed 0.6. The Be content in two-mica granite is ~13 ppm. If $f=0.4$, from Eq. 2, we can calculate that the Be content in the initial magma is ~30 ppm, and then we can work out that the Be content in residual magma is ~60 ppm based on Eq. 1. Then we can

use the Be content in the beryl-bearing muscovite granite to calculate the fractional degree in the second stage. The mass of the fluid and the Be content in fluid are gained via the mass balance. Rayleigh fractional calculations show that:

- a. the content of Be in the initial magma forming the Askartor deposit is as high as 30 ppm, which is 10 times of the average Be content in the upper crust (Be = ~3 ppm in upper crust, Taylor and McLennan, 1995). This value is similar to the Be



content of the less-altered tuffs and pumices from the Macusani Province, Peru (28 ± 9 ppm, with a high of 37 ppm, Noble et al., 1984). These rhyolites are S-type in overall chemical character with high $^{87}\text{Sr}/^{86}\text{Sr}$, strongly peraluminous composition, and trace element patterns that follow from an abundance of argillic or micaceous material at the source (Pichavant et al., 1988). Partial melting of a typical pelitic mica schist with 3 ppm Be, which is composed of muscovite, biotite, plagioclase, and quartz, will yield a content of 4–6 ppm Be in melt (Evensen and London, 2002), so, the pre-enrichment of Be in the source will restrict the mineralization of Be.

- b. The initial magma is fluid saturated after the crystallization of 60%, and the residual magma contains ~60 ppm Be. After that, the system changed from pure magma (+crystal) stage to magma-hydrothermal transition stage.

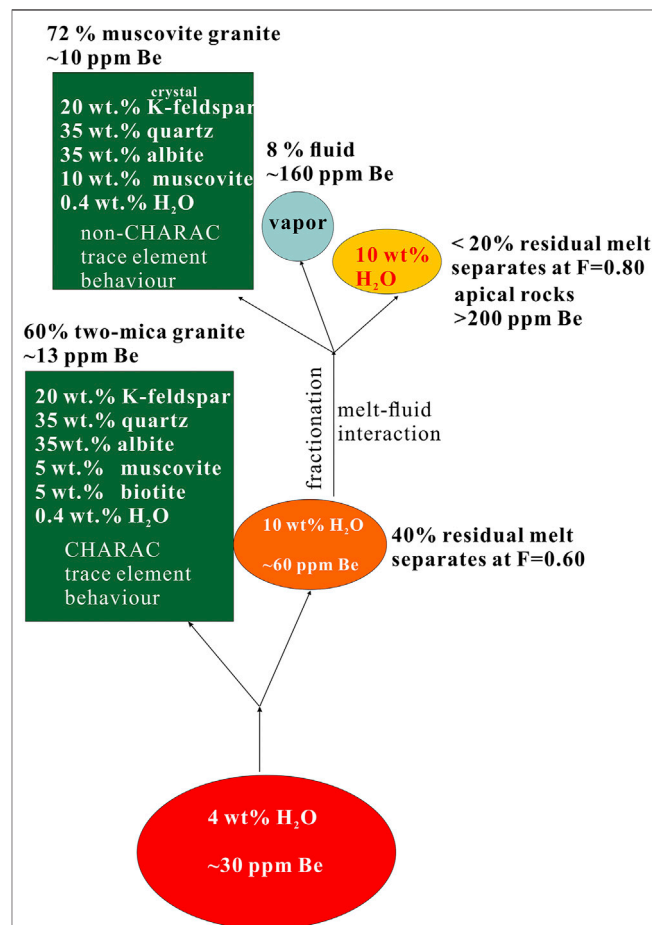


FIGURE 11 | A simple mineralization model for Askartor Be-Mo deposit.

This model is based on the fractionation crystallization. The partition coefficients of Be between minerals and melts are cited from Evensen and London (2002): $D^{\text{K-feldspar/melt}} = 0.14$; $D^{\text{quartz/melt}} = 0.24$; $D^{\text{albite/melt}} = 0.19$; $D^{\text{muscovite/melt}} = 1.35$; $D^{\text{biotite/melt}} = 0.54$; the mineral proportions are close to the real mineral proportions of rocks, which are typical of mica granite systems. Based on the inclusions, the emplacement pressure and temperature of the rocks from Askartor Be-Mo deposit are ~500 MPa and 800°C Ding (2016), so the H_2O content in the initial magma was ~4 wt% and the H_2O solubility in melt at this condition was 10 wt% Holtz et al. (2001).

- c. When this smaller volume of magma has reached ~80% solidification, then the residual magma could achieve beryl saturation ($\text{Be} > 200 \text{ ppm}$), assuming that it could be efficiently extracted to produce beryl-bearing muscovite granite and its overlying pegmatoid shell.
- d. The Be content of the exsolution fluid is as high as 160 ppm. The partition coefficient of Be in coexisting fluid and melt is 0.8, which is consistent with that obtained from the inclusion data (e.g., 0.37 ± 0.43 , Zajacz et al., 2008).

CONCLUSION

- (1) the zircon U-Pb ages of the granodiorite, biotite granite, two-mica granite, muscovite granite and pegmatoid are 386.8 ± 2.6 , 385.4 ± 4.4 , 247.5 ± 2.2 , 231.4 ± 2.0 , and $220.6 \pm 1.6 \text{ Ma}$, respectively. The molybdenite Re-Os isochron age is 228.7 ± 7.1 , which coincides with the zircon U-Pb age of $220.6 \pm 1.6 \text{ Ma}$ of the pegmatoid orebody. The two-mica granite, muscovite granite, beryl-bearing muscovite granite and pegmatoid shell have close spatial and temporal relationships.
- (2) The highly fractionated element ratios of Y/Ho, Zr/Hf and Nb/Ta, plus the REE tetrad effect indicate the fluid exsolution occurs at the late stage of magma evolution and the muscovite granite experienced strong self-metasomatism.

REFERENCES

- Andersen, T. (2002). Correction of common lead in U-Pb analyses that do not report 204Pb . *Chem. Geol.* 192 (1), 59–79. doi:10.1016/s0009-2541(02)00195-x
- Balouard, C., Poujol, M., Boulvais, P., Branquet, Y., Tartese, R., and Vigneresse, J.-L. (2016). Nb-Ta fractionation in peraluminous granites: a marker of the magmatic-hydrothermal transition. *Geology* 44 (3), 231–234. doi:10.1130/g37475.1
- Barton, M. D., and Young, S. (2002). Non-pegmatitic deposits of beryllium: mineralogy, geology, phase equilibria and origin. *Rev. Mineral. Geochem.* 50 (1), 591–691. doi:10.2138/rmg.2002.50.14
- Bau, M. (1996). Controls on the fractionation of isovalent trace elements in magmatic and aqueous systems: evidence from Y/Ho, Zr/Hf, and lanthanide tetrad effect. *Contrib. Mineral. Petrol.* 123 (3), 323–333. doi:10.1007/s004100050159
- Broussolle, A., Aguilar, C., Sun, M., Schulmann, K., Štípká, P., Jiang, Y., et al. (2018). Polycyclic Palaeozoic evolution of accretionary orogenic wedge in the southern Chinese Altai: evidence from structural relationships and U-Pb geochronology. *Lithos* 314–315, 400–424. doi:10.1016/j.lithos.2018.06.005
- Cai, K., Sun, M., Yuan, C., Zhao, G., Xiao, W., Long, X., et al. (2010). Geochronological and geochemical study of mafic dykes from the northwest Chinese Altai: implications for petrogenesis and tectonic evolution. *Gondwana Res.* 18 (4), 638–652. doi:10.1016/j.gr.2010.02.010
- Cai, K., Sun, M., Yuan, C., Zhao, G., Xiao, W., Long, X., et al. (2011a). Geochronology, petrogenesis and tectonic significance of peraluminous granites from the Chinese Altai, NW China. *Lithos* 127 (1), 261–281. doi:10.1016/j.lithos.2011.09.001
- Cai, K., Sun, M., Yuan, C., Zhao, G., Xiao, W., Long, X., et al. (2011b). Prolonged magmatism, juvenile nature and tectonic evolution of the Chinese Altai, NW China: evidence from zircon U-Pb and Hf isotopic study of Paleozoic granitoids. *J. Asian Earth Sci.* 42 (5), 949–968. doi:10.1016/j.jseas.2010.11.020
- Cai, K., Sun, M., Yuan, C., Zhao, G., Xiao, W., and Long, X. (2012a). Keketuohai mafic-ultramafic complex in the Chinese Altai, NW China: petrogenesis and geodynamic significance. *Chem. Geol.* 294–295, 26–41. doi:10.1016/j.chemgeo.2011.11.031
- Cai, K., Sun, M., Yuan, C., Xiao, W., Zhao, G., Long, X., et al. (2012b). Carboniferous mantle-derived felsic intrusion in the Chinese Altai, NW China: implications for geodynamic change of the accretionary orogenic belt. *Gondwana Res.* 22 (2), 681–698. doi:10.1016/j.gr.2011.11.008
- Cai, K., Sun, M., Jahn, B.-M., Xiao, W., Long, X., Chen, H., et al. (2016). Petrogenesis of the permian intermediate-mafic dikes in the Chinese Altai, northwest China: implication for a postaccretion extensional scenario. *J. Geol.* 124 (4), 481–500. doi:10.1086/686464
- Chen, B., and Jahn, B.-M. (2002). Geochemical and isotopic studies of the sedimentary and granitic rocks of the Altai orogen of Northwest China and their tectonic implications. *Geol. Mag.* 139 (1), 1–13. doi:10.1017/S0016756801006100
- Chen, J.-F. (2011). Geochemistry of the plate part in Altai No.3 pegmatite and its formation and evolution. Master's thesis. Beijing (China): University of Chinese Academy of Sciences.
- Ding, X., Li, J.-K., Ding, J.-G., Wang, S., Liu, Y.-C., and Wang, X. (2016). Molybdenite Re-Os isochron age and geological implication in Asikaerte Be-Nb-Mo deposit of Xinjiang. *J. Guilin Univ. Technol.* 36 (1), 60–65. doi:10.3969/j.issn.1674-9057.2016.01.009 [in Chinese, with English summary].
- Ding, X. (2016). Ore-forming mechanism of Askartor granite type beryllium deposit in Xinjiang, China. Master's thesis. Wuhan (China): China University of Geosciences.
- Du, A., Wu, S., Sun, D., Wang, S., Qu, W., Markey, R., et al. (2004). Preparation and certification of Re-Os dating reference materials: molybdenites HLP and JDC. *Geostand. Geoanalyt. Res.* 28 (1), 41–52. doi:10.1111/j.1751-908X.2004.tb01042.x
- Evensen, J. M., and London, D. (2002). Experimental silicate mineral/melt partition coefficients for beryllium and the crustal Be cycle from migmatite to pegmatite. *Geochim. et Cosmochim. Acta* 66 (12), 2239–2265. doi:10.1016/s0016-7037(02)00889-x
- Foley, N. K., Jaskula, B. W., Piatak, N. M., and Schulte, R. F., II (2017). “Beryllium,” in *Critical mineral resources of the United States-economic and environmental geology and prospects for future supply*. Editors K. J. Schulz, J. H. DeYoung, R. R. Jr Seal, and D. C. Bradley (Reston, VA: U.S. Geological Survey Professional Paper), 797.
- Holtz, F., Johannes, W., Tamic, N., and Behrens, H. (2001). Maximum and minimum water contents of granitic melts generated in the crust: a
- (3) Rayleigh fractional calculations show that the Askartor Be-Mo deposit is the product of multistage fractional crystallization of initial Be-enriched magma.

DATA AVAILABILITY STATEMENT

The original contributions presented in the study are included in the article/Supplementary Material, further inquiries can be directed to the corresponding authors.

AUTHOR CONTRIBUTIONS

TY, ZH, and LZ-H designed the study and Participated in field work, TY and LZ-H analysize the sample and acquired the data, All authors contributed to the writing of the manuscript, and read and approved the final version.

FUNDING

The study is supported by the National Science Foundation of China (No. 91962222).

- reevaluation and implications. *Lithos* 56 (1), 1–14. doi:10.1016/s0024-4937(00)00056-6
- Icenhower, J., and London, D. (1995). An experimental study of element partitioning among biotite, muscovite, and coexisting peraluminous silicic melt at 200 MPa (H_2O). *Am. Mineral.* 80 (11–12), 1229–1251. doi:10.2138/am-1995-11-1213
- Irber, W. (1999). The lanthanide tetrad effect and its correlation with K/Rb, Eu/Eu*, Sr/Eu, Y/Ho, and Zr/Hf of evolving peraluminous granite suites. *Geochim. et Cosmochim. Acta* 63 (3–4), 489–508. doi:10.1016/s0016-7037(99)00027-7
- Jiang, Y., Sun, M., Zhao, G., Yuan, C., Xiao, W., Xia, X., et al. (2010). The 390 Ma high-T metamorphic event in the Chinese Altai: a consequence of ridge-subduction?. *Am. J. Sci.* 310 (10), 1421–1452. doi:10.2475/10.2010.08
- Li, P., Yuan, C., Sun, M., Long, X., and Cai, K. (2015). Thermochronological constraints on the late Paleozoic tectonic evolution of the southern Chinese Altai. *J. Asian Earth Sci.* 113, 51–60. doi:10.1016/j.jseas.2014.11.004
- Liu, Y., Hu, Z., Gao, S., Günther, D., Xu, J., Gao, C., et al. (2008). *In situ* analysis of major and trace elements of anhydrous minerals by LA-ICP-MS without applying an internal standard. *Chem. Geol.* 257 (1), 34–43. doi:10.1016/j.chemgeo.2008.08.004
- London, D., and Evensen, J. M. (2002). Beryllium in silicic magmas and the origin of beryl-bearing pegmatites. *Rev. Mineral. Geochem.* 50 (1), 445–486. doi:10.2138/rmg.2002.50.11
- Ludwig, K. (2003). *User's manual for Isoplot 3.00: a geochronological toolkit for microsoft excel*. Berkeley, CA: Berkeley Geochronology Center Special Publication, 74.
- Lv, Z.-H., Zhang, H., and Tang, Y. (2021). Anatexis origin of rare metal/earth pegmatites: evidences from the Permian pegmatites in the Chinese Altai. *Lithos* 380–381, 105865. doi:10.1016/j.lithos.2020.105865
- Lv, Z.-H., Zhang, H., Tang, Y., and Guan, S.-J. (2012). Petrogenesis and magmatic-hydrothermal evolution time limitation of Kelumute No. 112 pegmatite in Altay, Northwestern China: evidence from zircon UPb and Hf isotopes. *Lithos* 154 (0), 374–391. doi:10.1016/j.lithos.2012.08.005
- Ma, Z.-L., Zhang, H., Tang, Y., Lv, Z.-H., Zhang, X., and Zhao, J.-Y. (2015). Zircon U-Pb geochronology and Hf isotopes of pegmatites from the Kaluan mining area in the Altay, Xinjiang and their genetic relationship with the Halong granite. *Geochimica* 44 (1), 9–26. doi:10.19700/j.0379-1726.2015.01.002 [in Chinese, with English summary].
- Maniar, P. D., and Piccoli, P. M. (1989). Tectonic discrimination of granitoids. *Geol. Soc. Am. Bull.* 101, 635–643. doi:10.1130/0016-7606(1989)101<0635:tdog>2.3.co;2
- Middlemost, E. A. K. (1994). Naming materials in the magma/igneous rock system. *Earth Sci. Rev.* 37 (3), 215–224. doi:10.1016/0012-8252(94)90029-9
- Monecke, T., Dulski, P., and Kempe, U. (2007). Origin of convex tetrads in rare earth element patterns of hydrothermally altered siliceous igneous rocks from the Zinnwald Sn-W deposit, Germany. *Geochim. et Cosmochim. Acta* 71 (2), 335–353. doi:10.1016/j.gca.2006.09.010
- Monecke, T., Kempe, U., Monecke, J., Sala, M., and Wolf, D. (2002). Tetrad effect in rare earth element distribution patterns: a method of quantification with application to rock and mineral samples from granite-related rare metal deposits. *Geochim. et Cosmochim. Acta* 66 (7), 1185–1196. doi:10.1016/s0016-7037(01)00849-3
- Noble, D. C., Vogel, T. A., Peterson, P. S., Landis, G. P., Grant, N. K., Jezek, P. A., et al. (1984). Rare-element-enriched, S-type ash-flow tuffs containing phenocrysts of muscovite, andalusite, and sillimanite, southeastern Peru. *Geology* 12 (1), 35–39. doi:10.1130/0091-7613(1984)12<35:rsatcp>2.0.co;10.1130/0091-7613(1984)12<35:rsatcp>2.0.co;2
- Pichavant, M., Kontak, D. J., Herrera, J. V., and Clark, A. H. (1988). The miocene-pliocene Macusani volcanics, SE Peru. *Contrib. Mineral. Petro.* 100 (3), 300–324. doi:10.1007/BF00379741
- Qi, L., Hu, J., and Gregoire, D. C. (2000). Determination of trace elements in granites by inductively coupled plasma mass spectrometry. *Talanta* 51 (3), 507–513. doi:10.1016/s0039-9140(99)00318-5
- Qin, K.-Z., Guo, Z.-l., Shen, M.-D., Tang, D.-M., Zhou, Q.-F., Wang, C.-L., et al. (2013). Typer, intrusive and mineralization ages of pegmatite rare-element deposits in Chinese Altay. *Xinjiang Geol.* 31, 1–7. [in Chinese, with English summary].
- Ren, B.-Q., Zhang, H., Tang, Y., and Lv, Z.-H. (2011). LA-ICPMS U-Pb zircon geochronology of the Altai pegmatites and its geological significance. *Acta Mineral. Sin.* 31 (3), 587–596. doi:10.16461/j.cnki.1000-4734.2011.03.041 [in Chinese, with English summary].
- Rickwood, P. C. (1989). Boundary lines within petrologic diagrams which use oxides of major and minor elements. *Lithos* 22 (4), 247–263. doi:10.1016/0024-4937(89)90028-5
- Shannon, R. D. (1976). Revised effective ionic radii and systematic studies of interatomic distances in halides and chalcogenides. *Acta Cryst. Sect. A* 32 (5), 751–767. doi:10.1107/s0567739476001551
- Smoliar, M. I., Walker, R. J., and Morgan, J. W. (1996). Re-Os ages of group IIA, IIIA, IVA, and IVB iron meteorites. *Science* 271 (5252), 1099–1102. doi:10.1126/science.271.5252.1099
- Stepanov, A. S., and Hermann, J. (2013). Fractionation of Nb and Ta by biotite and phengite: implications for the “missing Nb paradox”. *Geology* 41 (3), 303–306. doi:10.1130/g33781.1
- Sun, M., Yuan, C., Xiao, W., Long, X., Xia, X., Zhao, G., et al. (2008). Zircon U-Pb and Hf isotopic study of gneissic rocks from the Chinese Altai: progressive accretionary history in the early to middle Palaeozoic. *Chem. Geol.* 247 (3), 352–383. doi:10.1016/j.chemgeo.2007.10.026
- Sun, S.-S., and McDonough, W. F. (1989). Chemical and isotopic systematics of oceanic basalts: implications for mantle composition and processes. *Geol. Soc. London Spec. Publ.* 42 (1), 313–345. doi:10.1144/gsl.sp.1989.042.01.19
- Taylor, S. R., and McLennan, S. M. (1995). The geochemical evolution of the continental crust. *Rev. Geophys.* 33 (2), 241–265. doi:10.1029/95rg00262
- Tong, Y., Wang, T., Jahn, B.-M., Sun, M., Hong, D.-W., and Gao, J.-F. (2014). Post-accretionary permian granitoids in the Chinese Altai orogen: geochronology, petrogenesis and tectonic implications. *Am. J. Sci.* 314 (1), 80–109. doi:10.2475/01.2014.03
- Wang, C.-L., Qin, K.-Z., Tang, D.-M., Zhou, Q.-F., Shen, M.-D., Guo, Z.-L., et al. (2015). Geochronology and Hf isotope of zircon for the Arskartor Be-Nb-Mo deposit in Altay and its geological implication. *Acta Petrol. Sin.* 31 (8), 2337–2352.
- Wang, T., Hong, D. W., Jahn, B. M., Tong, Y., Wang, Y. B., Han, B. F., et al. (2006). Timing, petrogenesis, and setting of Paleozoic synorogenic intrusions from the Altai Mountains, Northwest China: implications for the tectonic evolution of an accretionary orogen. *J. Geol.* 114 (6), 735–751. doi:10.1086/507617
- Wang, T., Jahn, B.-M., Kovach, V. P., Tong, Y., Hong, D.-W., and Han, B.-F. (2009). Nd-Sr isotopic mapping of the Chinese Altai and implications for continental growth in the central asian orogenic belt. *Lithos* 110 (1), 359–372. doi:10.1016/j.lithos.2009.02.001
- Wang, T., Tong, Y., Jahn, B.-M., Zou, T.-R., Wang, Y.-B., Hong, D.-W., et al. (2007). SHRIMP U-Pb Zircon geochronology of the Altai No. 3 Pegmatite, NW China, and its implications for the origin and tectonic setting of the pegmatite. *Ore Geol. Rev.* 32 (1–2), 325–336. doi:10.1016/j.oregeorev.2006.10.001
- Windley, B. F., Kröner, A., Guo, J., Qu, G., Li, Y., and Zhang, C. (2002). Neoproterozoic to Paleozoic geology of the Altai orogen, NW China: new zircon age data and tectonic evolution. *J. Geol.* 110 (6), 719–737. doi:10.1086/342866
- Xiao, W., Han, C., Yuan, C., Sun, M., Lin, S., Chen, H., et al. (2008). Middle cambrian to permian subduction-related accretionary orogenesis of northern Xinjiang, NW China: implications for the tectonic evolution of central asia. *J. Asian Earth Sci.* 32 (2), 102–117. doi:10.1016/j.jseas.2007.10.008
- Xiao, W., Windley, B. F., Huang, B. C., Han, C. M., Yuan, C., Chen, H. L., et al. (2009). End-Permian to mid-Triassic termination of the accretionary processes of the southern Altaids: implications for the geodynamic evolution, Phanerozoic continental growth, and metallogeny of Central Asia. *Int. J. Earth Sci.* 98 (6), 1189–1217. doi:10.1007/s00531-008-0407-z
- Xiao, W., Windley, B. F., Han, C., Liu, W., Wan, B., Zhang, J. e., et al. (2018). Late Paleozoic to early Triassic multiple roll-back and oroclinal bending of the Mongolia collage in Central Asia. *Earth Sci. Rev.* 186, 94–128. doi:10.1016/j.earscirev.2017.09.020
- Xiao, W., Windley, B. F., Sun, S., Li, J., Huang, B., Han, C., et al. (2015). A tale of amalgamation of three permo-triassic collage systems in central asia: oroclines, sutures, and terminal accretion. *Annu. Rev. Earth Planet. Sci.* 43 (1), 477–507. doi:10.1146/annurev-earth-060614-105254
- Yang, F.-Q., Zhang, Z.-l., Wang, R., Li, Q., Ding, J.-G., Su, Z.-h., et al. (2018). Geological characteristics and metallogenesis of rare metal deposits in Altay, Xinjiang. *Geotecton. et Metallog.* 42 (6), 1010–1026. doi:10.16539/j.ddgzyckx.2018.06.006 [in Chinese, with English summary].

- Yin, R., Wang, R. C., Zhang, A.-C., Hu, H., Zhu, J. C., Rao, C., et al. (2013). Extreme fractionation from zircon to hafnon in the Koktokay No. 1 granitic pegmatite, Altai, Northwestern China. *Am. Mineral.* 98 (10), 1714–1724. doi:10.2138/am.2013.4494
- Yuan, C., Sun, M., Xiao, W., Li, X., Chen, H., Lin, S., et al. (2007). Accretionary orogenesis of the Chinese Altai: insights from paleozoic granitoids. *Chem. Geol.* 242 (1), 22–39. doi:10.1016/j.chemgeo.2007.02.013
- Zajacz, Z., Halter, W. E., Pettke, T., and Guillong, M. (2008). Determination of fluid/melt partition coefficients by LA-ICPMS analysis of co-existing fluid and silicate melt inclusions: controls on element partitioning. *Geochim. et Cosmochim. Acta* 72 (8), 2169–2197. doi:10.1016/j.gca.2008.01.034
- Zhang, A., Wang, R., Li, Y., Hu, H., Lu, X., Ji, J., et al. (2008). Tourmalines from the Koktokay No.3 pegmatite, Altai, NW China: spectroscopic characterization and relationships with the pegmatite evolution. *EJM* 20 (1), 143–154. doi:10.1127/0935-1221/2008/0020-1779
- Zhang, H., Lv, Z.-H., and Tang, Y. (2019). Metallogeny and prospecting model as well as prospecting direction of pegmatite-type rare metal ore deposits in Altay orogenic belt, Xinjian. *Mineral. Deposits* 38 (4), 792–814. doi:10.16111/j.0258-7106.2019.04.008 [in Chinese, with English summary].
- Zhang, Y.-F., Lin, X.-W., Zhao, Y.-M., Guo, Q.-M., and Zhao, D.-C. (2017). Geochronology and geochmeistry of granitoids of Ascalt beryllium deposit in Qinghe County, Northern Xinjiang. *Mineral. Deposits* 36 (3), 643–658. doi:10.16111/j.0258-7106.2017.03.007 [in Chinese, with English summary].
- Zou, T.-R., Chao, H.-Z., and Wu, B.-Q. (1988). Orogenic and anorogenic granitoids of Altay Mountains of Xinjiang and their discrimination criteria. *Acta Geol. Sin.* 2 (1), 45–64. doi:10.1111/j.1755-6724.1989.mp2001005.x
- Zou, T.-R., and Li, Q.-C. (2006). *Rare and rare earth metallic deposits in Xinjiang*. Beijing, China: Beijing: Geological Publishing House [in Chinese, with English summary].

Conflict of Interest: The authors declare that the research was conducted in the absence of any commercial or financial relationships that could be construed as a potential conflict of interest.

Copyright © 2021 Yong, Hui and Zheng-Hang. This is an open-access article distributed under the terms of the Creative Commons Attribution License (CC BY). The use, distribution or reproduction in other forums is permitted, provided the original author(s) and the copyright owner(s) are credited and that the original publication in this journal is cited, in accordance with accepted academic practice. No use, distribution or reproduction is permitted which does not comply with these terms.